THE EFFECT OF ALIGNED POROUS NANOFIBERS ON FILTER EFFICIENCY AND PRESSURE DROP

USMAN ALI

A THESIS SUBMITTED TO
THE FACULTY OF GRADUATE STUDIES
IN PARTIAL FULFILLMENT OF THE REQUIREMENTS
FOR THE DEGREE OF
MASTER OF APPLIED SCIENCE

GRADUATE PROGRAM IN MECHANICAL ENGINEERING
YORK UNIVERSITY
TORONTO, ONTARIO

DECEMBER 2023

ABSTRACT

Masks, vital for submicron filtration, face a trade-off between enhanced when increasing filter efficiency and, an increased pressure drop, impacting user comfort during physical activities leading to difficulty breathing. Polycaprolactone (PCL) and Nylon masks electrospun with humidity control, was investigated. Optimal conditions emerged with a 10% PCL solution by weight in a chloroform and dimethylformamide mix (8:2 ratio), collected at 500 RPM, producing highly efficient aligned porous fibers. Conversely, Nylon failed to yield porous fibers under any tested combination of parameters.

Our findings reveal a filtration efficiency range for porous aligned PCL fibers from 6% for 0.3 μm particles up to 42% at 5 μm, accompanied by a minimal pressure drop of 7 Pa. Introducing humidity proved effective in manufacturing porous nanofibers within a conventional electrospinning setup, offering promise for exploring diverse materials. The material's distinct behavior suggests a broad avenue for the development of oriented multilayered mask application.

ACKNOWLEDGMENTS

I express my deepest gratitude to my supervisor, Dr. Aleksander Czekanski, for his continuous guidance and immense support. I want to thank my committee member, Dr. Reza Rizvi, for his input into my project. I want to recognize Dr. Magdalena Jaklewicz and the Advanced Light and Electron Microscopy Facility for their extensive help with the SEM images. I want to thank my colleagues in IDEA Lab, who guided and supported me throughout my studies, making the process easier. I want to acknowledge my family, who cared for me and helped me through the years, and with them, I made it this far. Lastly, I would like to thank the Mechanical Engineering Department staff for their continual help and company through this process.

TABLE OF CONTENTS

LIST OF TABLES

LIST OF FIGURES

Chapter 1 Introduction

Summary: In this chapter, the problem and the justification for this study are introduced. Then, the research objectives are presented along with an outline of the thesis.

1.1 Face Filtering Masks

Face filtering masks, typically called just masks, are defined as filter material covering the nose and mouth of a user. These masks function to capture particles breathed in or out of the user. We get two use cases from this function: protecting the user from externally unwanted particles and preventing the expulsion of undesirable particles. The performance of these masks depends on the type of mask and the materials used in its construction.

Classification methods for masks fall into their performance or intended use. For example, the N95 mask dictates a specific product performance requirement. Masks built for personal protective equipment can also be classified as ‘surgical’ or ‘medical’ grade’ masks,’ with different performance requirements than N95 ones. More recently, masks produced to fill the demand during the pandemic were classified as ‘non-medical commercial masks’ with little to no performance requirements.

1.2 Justification of Study

In recent years, there has been a notable surge in both academic and practical interest in mask manufacturing. This heightened attention is primarily driven by the imperative to improve filtration efficiency and address escalating concerns about ultrafine air particles and viruses. This surge is reflected in the substantial increase in academic publications, with over 231 papers published in the past two years relating to both electrospinning and masks.

A crucial aspect of this intensified scrutiny in mask manufacturing is the utilization of electrospinning as a dominant technique. Electrospinning has gained significant recognition due to its inherent capability to produce submicron and nanoscale fibers, a feature essential for enhancing filter efficiency. This method has gained particular prominence in research due to its versatility and wide area of applications.

Much existing research has focused on investigating specific materials and non-woven fiber configurations, with limited exploration of aligned nanofibers and surface featured fiber surfaces. This unexplored research holds promise as it may improve mask production by improving filtration efficiency and pressure drop. Environmental impact has also seen attention in the form of reusability and biodegradability studies.

Given these emerging developments, this thesis aims to investigate aligned porous nanofibers and their potential applications in face-filtering respirators. This research seeks to provide novel insights within the field and advance the efficiency and pressure drop of existing face masks.

1.3 Research Objectives

In this research, we study the effect of fiber morphology on filter performance. More specifically, the collective impact of aligned porous nanofibers on pressure drop and filter efficiency. We have broken down into three research objectives:

1. Determine material process parameters for aligned porous nanofibers

2. Develop test apparatus and sequence for nanofiber material performance

3. Evaluate mask performance of nanofiber material

1.4 Thesis Outline

The thesis covers seven chapters, starting with the introduction presented here. **Chapter 2** comprehensively reviews the recent and relevant literature on face-filtering mask research and the electrospinning process while identifying gaps in the literature. **Chapter 3** lays out the methodological approaches used to carry out and complete the different research objectives. **Chapter 4** investigates the effect of various parameters on fiber morphology to optimize the manufacturing process. **Chapter 5** presents the design process and testing of an aerosol tester. Face filtering masks are tested and analyzed on this aerosol tester in **Chapter 6**, where different manufacturing process parameters in the filter performance are evaluated. Finally, **Chapter 7** summarizes research contributions and suggests new studies.

Chapter 2 Literature Review

Summary: In this chapter, first, the literature regarding mask classification, testing standards, and test setups is presented. Second, an overview of manufacturing methods to highlight a favorable technique is discussed. Third, the details on manufacturing parameters and their effects on fiber production. Finally, the latest electrospinning techniques are reviewed for creating shaped fibers.

2.1 Introduction to Masks

Masks can be medical, commercial, or retrofit. Medical masks aim to meet the needs of healthcare workers by preventing the escape of cough and sneeze particles from the user and protecting them from bacteria, blood, and other bodily fluids. Typically, medical masks consist of three layers: an inner hydrophilic layer to prevent the passage of cough and sneeze particles, a middle filtering layer, and an outer hydrophilic layer to protect against bodily fluids like blood. Industrial masks protect the user from airborne dangers in the workplace, like dust or hazardous material, regulated by governing bodies such as the National Institute for Occupational Safety and Health (NIOSH). NIOSH taxonomy uses letter and number notation such as N, P, R, and 90%, 95%, and 99%. For example, N95 indicates a mask's efficiency rating of 95% for particles as small as 0.3 μm while not being resistant to oil. The N denotes the mask materials resistant to oil, with N being non resistance, R somewhat resistant, and P being oil proof. Retrofit masks are made from materials not intended initially for filtration applications, such as silk, polyester, and cotton blends. These became popular with the surge of demand for masks during Covid.

2.1.1 Filtering Methods

Face masks are a barrier between the user and their environment, preventing the intrusion of unwanted bacteria, particles, and contaminants [1]. Air can pass through while capturing unwanted contaminants through four main processes: interception, inertial impaction, diffusion, and electrostatic attraction [2]. These captured particles are typically categorized into macro, micro, and nanoscale sizes.

Interception involves capturing particles larger than the pores in the barrier material. The size of the captured particle depends on the pore size, with typical particle sizes being 600 nm or more.

Inertial impaction captures particles as they lose kinetic energy and collide with mask fibers [2]. The particles come to rest within the barrier material. The typical size range for particles stopped due to inertial impaction is between 300 nm and 600 nm. These particles may be similar in size to the barrier material's pores.

Diffusion occurs when particles are captured as they migrate into the barrier material without impacting or intercepting it [2]. The capture mechanism relies on the carrier medium, often air, slowing down, allowing particles to deposit in the barrier material. This mechanism is predominant in smaller barrier materials like nanofibers. It applies to particles below 300 nm, which can easily suspend themselves in the air among air molecules.

Electrostatic attraction captures particles due to the charge they carry compared to the barrier material [2]. The barrier material can either be charged or made of a material with an opposing charge. There is no specific size range for particles captured through electrostatic attraction.

2.1.2 Testing Methods

Traditionally, mask testing had similar requirements on different standards based on the application area. Organizations like the American Society for Testing and Materials International (ASTM) and NIOSH set testing parameters at levels similar to the expected or worst-case scenario. For example, surgical masks are certified by the Food and Drug Administration (FDA) but tested by the manufacturer [3]. Manufacturers have provided fluid resistance, particulate filtration efficiency (PFE), bacterial filtration efficiency (BFE), differential pressure (DP), and flammability for certification. The FDA has also certified surgical N95 masks through NIOSH certification. The N95 status was counted towards the filter efficiencies and differential pressure, leaving only fluid resistance and flammability to test. Manufacturers have gotten around the N95 certification by conducting tests using ASTM F2299 and ASTM F2101 for PFE and BFE tests. In Table 2-1, the literature shows significant variance in approach because the FDA only has a guidance document. Additionally, no mention had been made of the testing region, whether the whole mask or a section. The literature identified another method called viral filtration efficiency, which must be conducted on personal protective equipment (PPE), as confirmed by the FDA. This method had not been marked as a standard test protocol. However, it was regarded as one of the most efficient measures to prevent epidemic infections.

Table 2-1 Comparing test methods and parameters (reproduced from [3])

Test	Aerosol	Particle	Flow Rate	Time	Max
Method	Type	Size	(Face Velocity)	Time	Efficiency
NIOSH NaCl	NaCl	0.075 µm CMD (GSD <1.86)	85 L/min	Maximum penetration	100.00%
FDA-PFE	PS latex spheres (FDAGuidance Document)	0.1 µm (FDA Guidance Document)	0.5-25 cm/sec (ASTMF2299)	1-5 min Initial efficiency (ASTM F2299)	99.9% (ASTM F2299)
ASTM-PFE	Latex spheres	0.1 to 5.0 µm (Mono-disperse aerosol; MPS	0.5-25 cm/sec	1-5 min Initial efficiency	99.90%
FDA-BFE	Staphylococcus aureus (ASTM F2101)	3.0 ± 0.3 µm (MPS) (ASTM F2101)	28.3 L/min (ASTM F2101)	2 min aerosol exposure per test (ASTM 2101)	99.9% (ASTM F2101)
ASTM-BFE	Staphylococcus aureus bacteria	3.0 ± 0.3 µm MPS	28.3 L/min	2 min aerosol exposure per test	99.90%
VFE	PhiX174 virus	3.0 ± 0.3 µm MPS (adapted from ASTM F2101)	28.3 L/min (< 4.7 cm/sec) (per Nelson Labs)	Not Defined	99.9% (adapted from ASTM F2101)

2.1.3 Test Apparatus

Two approaches examined for testing filtration efficiency and pressure drop have been automated commercial testers [3] and lab-developed apparatuses [4]. In principle, both have the same methodology achieved in three steps: conditioning, sampling, and processing. The first step comprises particle generating, dilution, drying, and nebulizing air to contain specified particulates. Second, air samples around this flow, typical particle count, and pressure are taken. Third, sampled data is automatically or manually processed into PFE and DP reports, depending on the equipment.

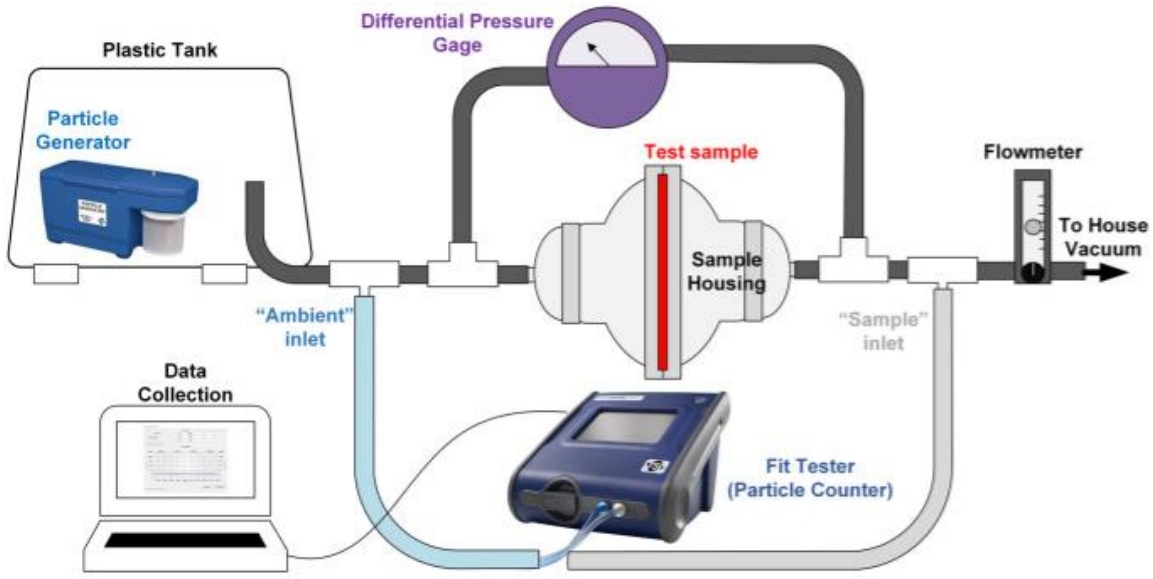

Figure 2-1 Low-cost test apparatus diagram (reproduced from [5])

2.1.4 Existing Masks

In the mask market, there is availability for surgical, commercial, and retrofit masks. Typical commercial masks are tight-fitting masks marketed to filter fine dust, such as N95 masks rated for debris up to 0.5 µm in size. Surgical masks are loose-fitting masks that prevent the spread of large droplets and germs. Some medical masks are available as tight-fitting with an N95 rating. Polypropylene is a common material for constructing both these masks using a melt-blowing process. Commercial masks are not limited to this material or method, as variants use fabrics such as cotton or cotton blends. Although the materials are the same or use similar production methods, the performance differs.

Table 2-2 Mask performance at differing flow rates (reproduced from [6])

Mask	Filtration Efficiency (%)	Pressure Drop (Pa)	Flow Rate (LPM)
N95	85.0%	2.2	35
Surgical	76.0%	2.5	35
N95 with Gap	94%	13.2	90
Surgical with Gap	61.0%	11.9	90

Typical retrofit masks consist of various household fabrics, commonly blends of cotton. The performance of these masks differs based on the construction of the fabric. Fabric construction is typically unwoven or woven and defined by threads per inch.

Table 2-3 Household material performance at two flowrates (reproduced from [6])

Item	Material	Weave	Filtration Efficiency (%)	Pressure Drop (Pa)	Flow (L/min)
Air Con. Filter	Polyester	Unwoven	12.8%	0.3	30
Coffee Filter	Paper	-	32.5%	7.7	30
Fabric	Silk	-	30.5%	31.6	30
Pillowcase	Cotton	200 Thread Count	16.2%	6.5	30
Pillowcase	Cotton	400 Thread Count	20.3%	7.8	30
Pillowcase	Polycotton	200 Thread Count	23.2%	7.5	30
Pillowcase	Polycotton	130 Thread Count	30.0%	4.0	30
Air Con. Filter	Polyester	Unwoven	11.3%	0.8	85
Coffee Filter	Paper	-	20.9%	28.2	85
Fabric	Silk	-	20.6%	108.7	85
Pillowcase	Cotton	200 Thread Count	13.4%	20.7	85
Pillowcase	Cotton	400 Thread Count	17.1%	24.6	85
Pillowcase	Polycotton	200 Thread Count	19.0%	23.5	85
Pillowcase	Polycotton	130 Thread Count	16.3%	11.5	85

Amongst retrofit mask materials, filtration performance is better when the material is packed more densely. The added benefit is that pressure drop remains low relative to surgical and commercial N95s. Testing the materials at increased flow rates to simulate exercising activities reveals that

filtration efficiency is lowered marginally. However, pressure drop increases drastically, with all materials showing a minimum increase of double the value tested at 35 LPM.

The filter performance of medical and commercial masks appeared higher than retrofit variants [6]. However, the pressure drop of the retrofit masks seems to sit at a lower level, where the lower the pressure, the better it is. The current masks and available materials do not present any reasonable choice for material with a low-pressure drop and high filter efficiency [6]. As the filtering efficiency increases, so does the pressure drop. In the literature, no recent works define the acceptable level of pressure drop for a mask. Instead, untranslatable breathing resistance values are determined, such as 25 cm H_2O [7].

2.2 Manufacturing Methods

Manufacturers construct masks from a variety of materials. The type of mask determines its effectiveness, as well as the manufacturing method and material substructure. Face masks are a type of mask commonly used for single-use personal protective equipment applications. These consumer masks are manufactured using spun bonding, melt-blowing, and electrospinning, with the latter two achieving smaller fiber diameters [8]. Manufacturers use combined approaches to continuously create layered mask materials utilizing a sequential process starting with spun bonding, followed by a melt-blowing layer, topped with a spun bonding layer [9]. Spun bonding is not used standalone to create filter materials but for their ability to bond to other materials during manufacturing and retain hydrophobic and hydrophilic properties.

2.2.1 Spun Bonding

The spun bonding process is an extrusion process consisting of five operations: filament extrusion, drawing, quenching, lay down, and bonding [9]. The process starts with filament extrusion using

polymer powder or pellets in an extruder. Next, the molten polymer is drawn through a die block assembly (known as the 'spin pack') which extrudes thin filaments. These filaments are quenched in a zone of cool air, causing filament solidification. Attenuation follows, controlling the polymer molecular orientation and fiber diameter as it lays down onto a conveyor belt. The filaments then undergo bonding to make a robust and interconnected fabric utilizing thermal, chemical, or mechanical methods.

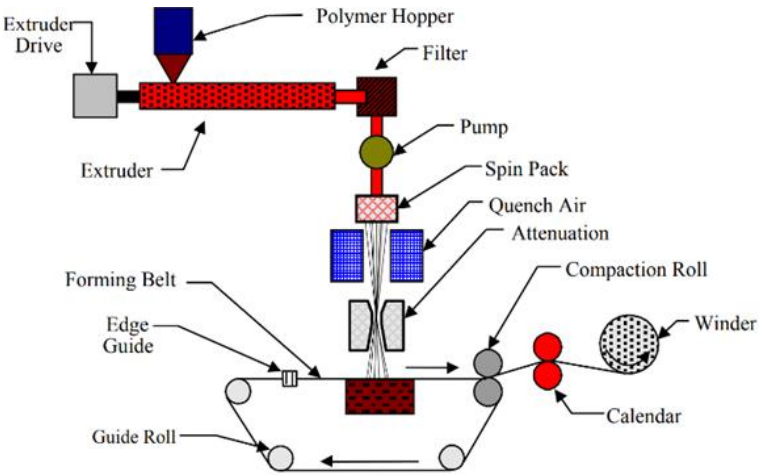

Figure 2-2 Schematic of spun bonding process (reproduced from [9])

Nylon filtering material can be spun bond, achieving an average fiber diameter of 17.64 ± 2.65 µm [10]. Filtration efficiency and pressure drop for a single spun bond layer was 4% with a 5 Pa drop, unusable for filtration but very breathable. Multiple materials can be combined, such as polyethylene and polypropylene, in equal parts to achieve a filter material with fiber sizes ranging between 14.13 to 15.03 µm. The performance achieved by this combination was 98.94% filter efficiency with a 37.92 Pa drop. The limitation of this process is the size of fibers that can quickly produced, often remaining in the micrometer scale. The setup of this process is also bulky, although the production is continuous, which is the only favorable trait.

2.2.2 Melt-Blowing

The melt-blowing process is a more straightforward extrusion process consisting of four operations: filament extrusion, attenuation, forming, and lay down [9]. The process starts with filament extrusion using polymer powder or pellets in an extruder. Next, the molten polymer is drawn through a melt-blown die using hot air, which extrudes thin filaments. These filaments are then attenuated by the hot air immediately after being drawn. Forming occurs when the hot air and molten filament mix with ambient air, causing stretching and reciprocating motion. The fibers solidify and travel toward a conveyor by hot air until they lie on it.

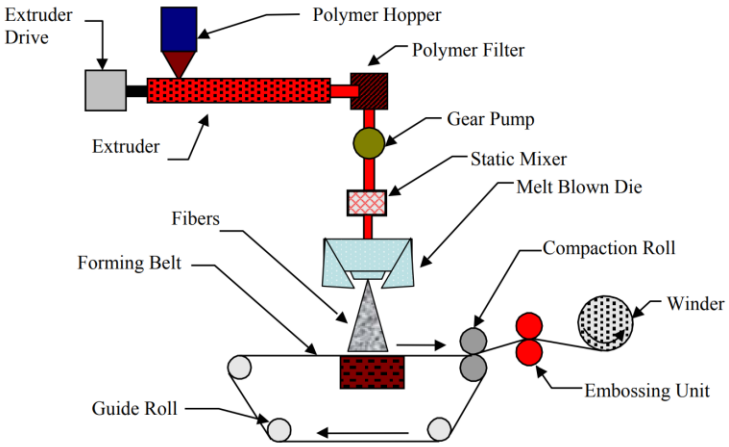

Figure 2-3 Schematic of melt blowing process (reproduced from [9])

Nylon can also be melt blown to achieve an average fiber diameter of 1.17 ± 0.38 µm [10]. The performance of a single melt-blown nylon layer was 32% filtration with an 84 Pa drop. The filtration efficiency is better in this process, but the pressure drop drastically climbs. Polypropylene melt-blown produces fibers with an average size of 1.6 µm with a pressure drop of 40 Pa [11], [12]. This material can be corona-charged to increase the filter performance. The lowest reported filtering efficiency was 72.33%, achieved by charging the filters with no reported pressure drop. Materials have been melt-blown over other materials, such as melt-blown polytetrafluoroethylene.

over conventional car cabin filters [13]. The result is a material with a single layer at 1.44 µm thick. Pore size was reported instead of fiber diameter, measuring an average of 0.318 µm. The achieved performance with this method was 95.48% filter efficiency with no reported pressure drop. The air permeability was reported instead at 66.218 cubic centimeters per second. Similar to spun bonding, the setups are complex. The fibers are not in the nanoscale, although performance was better than some retrofit masks.

2.2.3 Electrospinning

Electrospinning is a simple process consisting of 3 operations: pumping, charging, and collection [9]. The process begins with the polymer solution pumping through a needle conventionally with a blunt tip. Then, a high voltage gets applied to the needle, causing electrostatic charge buildup in the solution [14]. The charge changes the shape of the solution from a typical round liquid drop into a cone, commonly referred to as a Taylor Cone [15]. This effect is possible when the electrostatic forces overcome the surface tension of the solution. After the cone, the polymer solution forms a jet stream. The jet stream starts in a region of stable flow, leading to an unstable region whipping the jet in random directions [16]. The jet solidifies and is then deposited on a collector, static or dynamic. The type of collector will determine the fiber orientation.

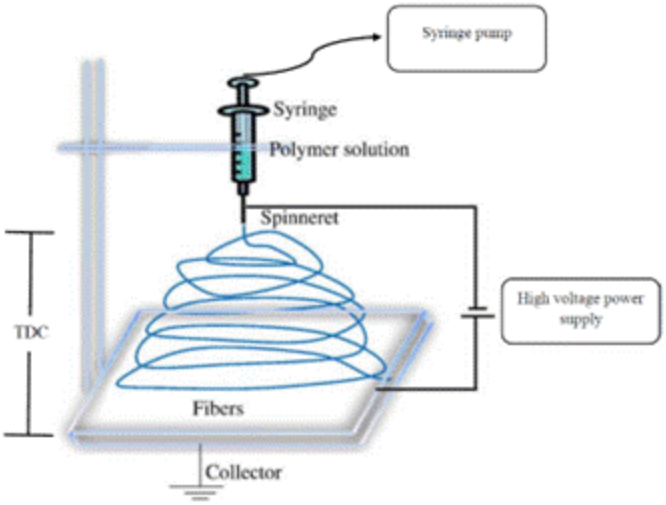

Figure 2-4 Schematic of the electrospinning process

Polycaprolactone (PCL) has been used to create material for filtration applications through electrospinning [17]. This material had an average fiber diameter below 150 nm, boosting the efficiencies of 99.99% filtration while holding a pressure drop of around 250 Pa. PCL has also been doped with metal nanoparticles to create a hybrid material [18]. The observed fiber sizes were between 408 nm and 589 nm, performing at efficiencies greater than 99% filtration, with a pressure drop of 34 Pa. Like melt blowing, materials can also be mixed to create hybrids. Polyvinyl alcohol and chitosan were electrospun to create a material with an average fiber diameter of 306 nm and 496 nm. The filtering efficiency achieved was 95%, with a pressure drop of 343.2 Pa.

The methods employed to manufacture masks can all produce some materials with high filtration efficiency or low-pressure drop. The filter efficiency of electrospun materials boosts the highest efficiency with varying results in pressure drop. This method seems to be the best method for this study to attain nanofibers.

2.3 Electrospinning Parameters Technique

Electrospinning contains many parameters specific to the polymer solution, the spinning process, and the environment [19]. The polymer solution is characterized by solvent mix, solvent volatility, dielectric constant, surface tension, concentration, conductivity, viscosity, and flow rate [20]. The process parameters are applied voltage, voltage polarity, the distance between tip to collector, nozzle diameter, and flow rate. The environment is characterized by relative humidity, temperature, atmospheric composition, and pressure.

2.3.1 Solution Parameters

Solvent Mix & Volatility

The solvent mix defines the composition of solvent(s) used in an electrospinning solution mix. Solvent volatility is the solvent's ability to evaporate quickly, specifically high evaporation rates at room temperature. The choice of solvents and their volatility affects the solutions ability to produce fibers and its surface morphology [21]. Solvents are categorized by their compatibility with the selected polymer. The classifications are insoluble, partially soluble, and soluble. Poor and high are further classifications that can be used to describe how well soluble solvents can dissolve the polymer. Solvent solubility is not directly correlated to solution ability to produce fibers as electrospinning can be done with a solution using a partially soluble solvent instead of soluble solvents alone. Secondary and tertiary solvents can change solution characteristics to improve printability, such as conductivity and viscosity [22]. Binary solvent solutions can also cause fiber features such as pores due to the solution solvents' different and rapid evaporation rates [23].

Dielectric Constant

The dielectric constant is the polymer solution's capacity to hold charge and differs amongst polymer and solvent combinations [24]. The dielectric constant affects the applied electric field (applied voltage) necessary for stable jetting of the polymer solution. Fiber diameter size decreases as the dielectric constant increases in a polymer solution. When the dielectric constant decreases, porosity in the fiber morphology increases in frequency [25].

Surface Tension

The polymer solutions' surface, as well as electrical conductivity, is a critical parameter for determining electrospinability [26]. When the surface tension is too high, the electrical conductivity can not produce static charge forces strong enough to shape the liquid solution. When the surface tension is too low, electro-spraying occurs instead of electrospinning, where the liquid cannot keep the form of a continuous jet stream and breaks into droplets.

Viscosity

The viscosity of the polymer solution is a crucial parameter for determining stable spinning [27]. When viscosity becomes excessively high, it leads to an excess of liquid, forming smaller fibers. Conversely, when viscosity is too low, the liquid behaves erratically, leading to clogging and larger fiber diameters.

Electrical Conductivity

The electrical conductivity of the solution is critical for ensuring the electrospinning process occurs. Electrical conductivity drives the Taylor cone and pulls the liquid stream into the spinning zone to form dry and uniform fibers. Increasing solution conductivity decreases the average fiber

size [28]. Older studies found that increasing electrical conductivity also decreases the formation of beads [29].

Concentration

Concentration is proportional to viscosity, surface tension, and electrical conductivity. It can be an excellent measure to control these parameters [30]. Increasing the concentration of the solute in the solution reduces viscosity, increases surface tension, and decreases electrical conductivity, making it more challenging to achieve successful electrospinning. This increase can, however, lead to an increase in fiber diameter and uniformity [31]. Conversely, lowering the concentration increases electrical conductivity, decreases surface tension, and makes the process easier to execute. However, there is a critical point at which fibers cease to be produced, and electro-spraying occurs instead.

2.3.2 Spinning Parameters

Flowrate

Flow rate plays a crucial role in controlling the amount of material produced and influences various parameters, including fiber size and hybrid density. It must be carefully controlled in conjunction with conductivity to ensure smooth electrospinning operation. Low flow rates are associated with smaller fiber sizes, while high flow rates result in larger fibers.

Applied Voltage & Polarity

The applied voltage serves as the driving force in the electrospinning process. Increasing voltage can lead to a decrease in fiber diameter [32]. However, too much voltage rapidly increases fiber diameter as large fibers form due to higher solution ejection. Flowrate must also be considered due to its ability to interfere with the effects of applied voltage. If the flow is fast, the solution has no

time to evaporate, leading to beading. This beading has been attributed to decreased electrical conductivity [33]. The flow rate must match the rate of ejection from the needle for stable operations.

Switching polarity between the needle and collector can result in differing deposition rates [34]. In some cases, with the traditional approach, attaching the collector to a negative terminal can create a stronger magnetic field, attracting the solution for collection. This approach benefits specific polymer-solvent systems where low electrical conductivity prevents grounding. It enhances fiber collection in low and high regions and aids in controlling morphological features such as fiber diameter.

Tip and Collector Distance

The tip-to-collective distance is adjusted to control the solvent evaporation before collecting the fiber [35]. Increasing the distance will allow more solvent to evaporate while decreasing the distance will allow less. The impact caused by this affects the average fiber diameter of the material [36].

Nozzle Diameter

The nozzle diameter controls the droplet size formed during electrospinning [37]. Increasing the diameter increases the size of the droplet and vice versa. The effect of this is that the average fiber size increases as the needle diameter increases. The increase can be associated with the surface tension increasing as the diameter decreases [18].

2.3.3 Environmental Parameters

Relative Humidity

The humidity of the environment in electrospinning controls the evaporation of the solvent during electrospinning [1]. Increasing the water molecules in the air can affect the fiber's solidification. The effect depends on whether the polymer is hydrosoluble or hydrophobic. For hydrosoluble polymers, increasing the humidity delays the formation and eventually causes no solidification. However, with hydrophobic polymers, evaporation is accelerated, causing the separation within the fiber. This acceleration can lead to thick and porous, rough, and wrinkled fibers in appearance due to the increased ejection of material. The formation of these fibers is driven by a process called induced phase change. This induced pace change can happen by vapor, temperature, and non-solvents.

Temperature

The environment's temperature also controls the evaporation rate during electrospinning [35]. The average fiber diameter decreases when the temperature increases, but this effect is not continuous and plateaus depending on the material.

2.4 Morphology and Alignment

The surface morphology of fibers resulting in porous, wrinkled, grooved, rough, nano-protrusion, and hollow features have been explored [38], [39]. The electrospinning mechanisms enabling these features can be categorized into breath figures, vapor-induced phase change, nonsolvent-induced phase change, and thermally induced phase change [40].

Figure 2-5 Graphical abstract of surface morphologies (reproduced from [38])

Breath figures rely on high relative humidity and a significant temperature drop. This drop is achieved using volatile solvents such as dichloromethane [41] and chloroform [42]. The rapid evaporation of the volatile solvent leads to fiber cooling, inducing water condensation. The water produces cavities upon drying, leaving a porous surface.

Vapor-induced phase separation (VIPS) also relies on high relative humidity and water vapor; however, the solvent choice changes to one with high volatility and poor water miscibility, such as dimethylformamide [43]. The solvent evaporates slowly, allowing time for the water to penetrate the fiber during the drying process. A porous structure is revealed upon the drying of the water.

Non-solvent-induced phase separation relies on a binary solvent solution to induce porosity. One of the solvents needs to be non-solvent to the polymer selected. The non-solvent acts like the water in VIPS, enabling the non-solvent to occupy space along the fiber. A cavity is formed upon evaporating, leaving a porous structure [44].

Finally, temperature-induced phase separation relies on a significant temperature drop. This effect can be done by collecting onto a cold collector. Researchers recently used this to produce porous PCL fibers [45]. Like breath figures, the solvent rapidly evaporates, leaving unique surface morphologies.

2.4.1 Porous Nanofibers

Polymers producing porous fibers have varying effects on fiber size and pore intensity. Polyvinylidene fluoride used at 7% weight in acetone produced porous and beaded fibers, averaging 181 nm in diameter [46]. Polymethyl methacrylate spun at 8% produced porous fibers averaged at 1.49 μm [47]. Polylactic acid was prepared with a binary solution of dichloromethane and dimethylformamide at 8% weight, resulting in 1.13 μm fibers [48]. Polystyrene fibers were prepared using a tertiary solution of camphene, tetraethoxysilane, and dimethylformamide [49]. With a 30% solution at a humidity between 50 and 70%, fibers ranging between 0.1 to 4 μm were observed. Polycaprolactone produced 3.29 μm fibers when prepared using cryogenic electrospinning at 27% weight in glacial acetic acid [50]. Polyamide 6, or Nylon, was prepared with formic acid and acetone mixed by volume at a ratio of 3 to 1 [51]. A concentration of 4% produced a range of fiber diameters from 400 nm to 1.7 μm.

The range of fiber diameters is significant for most materials. Single, double, and triple solvent solutions were used with humidity and temperature to attain porous fibers. The studies often tested

between one to three parameters: solution concentration, solvent ratios, humidity, and temperatures. Many polymer-solvent combinations have not been explored, meriting further investigation.

2.4.2 Alignment

The spinning of fibers into a random orientation is simpler than strands in a linear and parallel fashion. The degree of alignment is heavily influence by the methods employed to create them which is controlled by the collector [52]. Aligned fibers are produced with static collectors like parallel plates and parallel rings, while for dynamic collectors solid drums, and wire drums, mandrels and rotating disks. A dynamic drum was spun to collect aligned polylactic acid fibers producing a material with a filter efficiency of 99.99% and a pressure drop of 96 Pa compared to randomly oriented at 99.66% filtration with a 165 Pa [53]. Static parallel plates produced aligned polyacrylonitrile nanofibers resulting a material with a filtration efficiency of 81.98% and pressure drop of 125 Pa [54]. This is an improvement over the same material produced in a random orientation with a filtration efficiency of 68.91% and pressure drop of 103 Pa.

2.4.3 Surface Morphology Filtration Performance

Nano-protrusions were produced on cotton fibers using corn protein achieving a filter efficiency of 99.5% with a pressure drop of 194 Pa/g [55]. Wrinkled fibers were produced using polyacrylonitrile doped with tetraethyl orthosilicate reaching a filtration efficiency of 99% with a pressure drop of 350 Pa [56]. Porous polylactic acid fibers produced a filter material achieving a filter efficiency of 99.99% with low pressure drops between 110 Pa to 230 Pa [57]. Hollow fibers produced using polyvinylidene fluoride attained a filtration efficiency of 99.99% with a drop of 100 Pa.

2.4.4 Present Works

The morphology and orientation of fibers tested in filtration applications varies between random [17], aligned [54], smooth [18], porous [57], wrinkled [56], and protruded [55]. Each morphology produced does not employ a simple electrospinning process requiring additional post processing steps like doping [55]. Additionally, morphologies and aligned orientation are not studied in tandem. This leaves work to be done attempting to use simplified techniques to produce unique morphologies and in aligned orientations. This opens a new area of exploration for multi featured filter materials.

Chapter 3 Methodology

Summary: This chapter presents the methodology used in the study. The methods employed in this work are divided into three parts for each objective: the development of fiber morphology, material testing method, and material performance.

3.1 Fiber Morphology Determination

Fiber morphology is a blanket term used to refer to fiber diameter, surface, and orientation. It can be determined quantitatively or qualitatively, depending on the focus of the study. In this study, a sequential qualitative analysis is conducted in the form of microscopy to determine favorable features in the fibers. Four parameters will be varied to observe the effect. These results are selected for further study. The study parameters are solution concentration, collector speed, solvent ratio, and humidity. The solution concentration provides general insight into the fibers produced with the polymer solvent mix. Through microscopy, a favorable solution is determined for various collector speeds to observe fiber alignment. The speed required for alignment is then used with different solvent ratios and humidity to target the desired feature production in the fibers determined through microscopy.

3.1.1 Materials

Polycaprolactone (purchased from Sigma Aldrich) was selected for the study for its degradability property. Two solvents were used to prepare polymer solution mixes: liquid chloroform (purchased from Fisher Scientific) and dimethyl formamide (purchased from Sigma Aldrich).

3.1.2 Solution Preparation

The solution is comprised of a polymer with one or more solvents. Polymer pellets were measured by gram on a weight scale (by MetLab). The solvent is measured using a glass granular. Solvents are mixed in a 50 ml beaker with a magnetic stir bar and placed on a magnetic heat plate for mixing. Polymer pellets were added to the solvents and sealed with aluminum foil. The polymer solvent solution was left to mix for 12 hours minimum mechanically. Aluminum foil was removed and picked up by a syringe before being capped by a blunt needle.

3.1.3 Electrospinning Setup

Five components and two consumables make up the setup of a traditional electrospinning process. First, a high voltage power supply (purchased from Genvolt), syringe pump (purchased from New Era), drum collector (designed in-house), humidifier (purchased from Honeywell), and environment chamber (designed in-house). For consumables, 5ml luer lock syringes and 20-gauge blunt needles (purchased from McMaster Carr).

Figure 3-1 Overview of the components in the electrospinning setup

3.1.4 Electrospinning Operation

The parameters used for electrospinning were determined experimentally with the aid of literature to reduce iterations. The following parameters were fixed for comparative purposes during fiber morphology determination: needle gauge, flow rate, tip-to-collector distance, and applied voltage. Humidity and collector speed were varied to achieve the desired fiber and material properties. The high voltage power supply was set according to material, 6 kV for PCL. The syringe pump was set to 0.1 mL/h with a 5 mL syringe fitted with a 20 gauge blunt needle. The distance between the needle tip and the collector was 20 cm. Aluminum foil was wrapped on the drum collector to collect filter material. Drum collector speed was varied between 100 RPM for random and 500 RPM for aligned fiber orientations. The humidifier was turned on to produce porous fiber filter material regulating the environment between 0 – 100% relative humidity. Two types of samples

were produced, differentiated by operation time. A shorter 30-minute spin was set up for microscopy, while a 3-hour spin was set up for mask performance testing.

3.1.5 Microscopy

Filter material was characterized using SEM and ImageJ software. Filter samples less than 10 x 10 mm were cut from the filter material sheet. Filter samples were sputter coated with platinum at 35 mA for 15 seconds (using a Denton Vacuum Desk V). Photos were taken on SEM and imported into ImageJ for the manual measure. The minimum and maximum sizes of fibers were photographed. Attention was given to photographing anomalies.

The photographs were used to select favorable fibers when investigating solution concentrations, collector speed, solvent ratios, and humidity. The solution concentration investigation aimed to produce smooth nanometer fibers as a starting point for further fiber development. The collector speed looked at producing fibers that are mostly aligned. Categorizing fibers determined this production as random, linear, and aligned. Random fibers were categorized as having no linearity rather than a curving path. Linear fibers were grouped as straight but did not align with the collection direction. Aligned fibers were sorted as linear fibers aligned with the redirection of collection. For each speed all fibers in the photo frames were analyze with a minimum of 25 fibers. This speed was used with different solvent ratios and humidity to investigate fiber morphological effects. Three solvent ratios and humidities were selected from this study based on the literature review. Solvent ratios will increase by 1 part of a secondary solvent out of 10 parts (9:1, 8:2, 7:3). Humidity was relative to room temperature and was set at 25%, 50%, and 75%.

3.2 Material Test Development

The development of material tests depends on the application of the material, in this case, aerosol filtration. The primary metrics are particle filtration efficiency and pressure drop. A simple apparatus was constructed to achieve the measurement of these metrics. Following the literature for a typical aerosol setup, we designed an apparatus that preconditions air and then tests particle count upstream and downstream while taking the differential pressure across the mask. Verification was achieved by running particle distribution tests compared against the manufacturers' data.

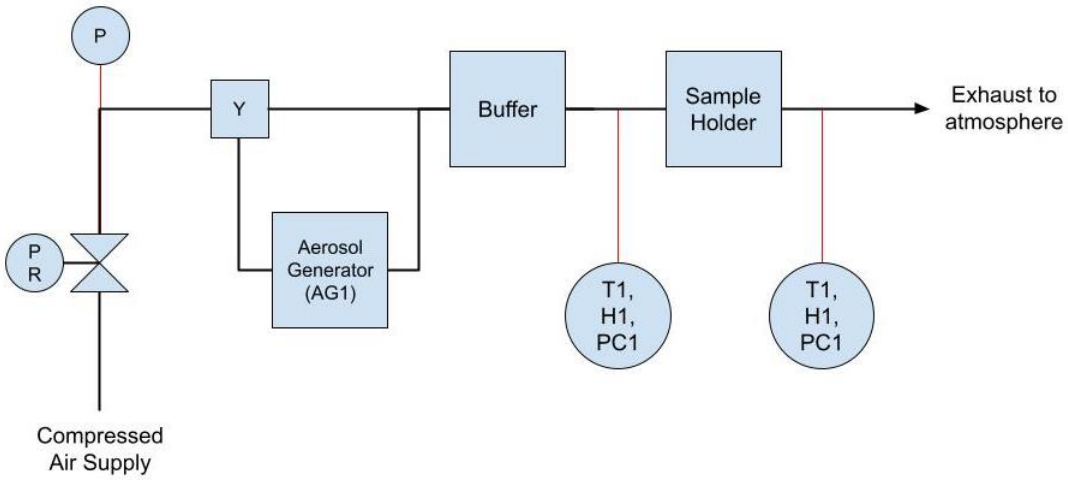

Figure 3-2 Aerosol testing apparatus schematic

3.2.1 Particle Distribution

The particle distribution is a graphical method of displaying the range of particles produced at a given flow rate. This graph also aims to understand the quantity of aerosols passing through the mask. Particle distributions are also used to calculate filtration efficiency graphs that compare the difference of particles before and after the material in a flow condition. The trend in these graphs should display a Gaussian distribution to exhibit good particle generation. This distribution also

demonstrated the size and range of particles used in testing which is limited by the particle counters capabilities.

3.3 Filter Material Performance Evaluation

Filter material performance refers to a material's particle filtration efficiency and pressure drop for the air application. It can be determined quantitatively in the form of an aerosol test. ASTM standard F2299 can be mimicked for submicron particle filtration efficiency for this testing.

3.3.1 Sample Preparation

Samples were cut to fit the opening of PVC fittings for an observable test area of 2 inches in diameter. A template was traced onto the top layer and cut out with scissors for existing surgical and non-surgical masks. For thinner samples, such as electrospun fibers, a frame was produced of polylactic acid in a 3D printer. The fiber membrane was transferred to the frame and secured with double-sided tape.

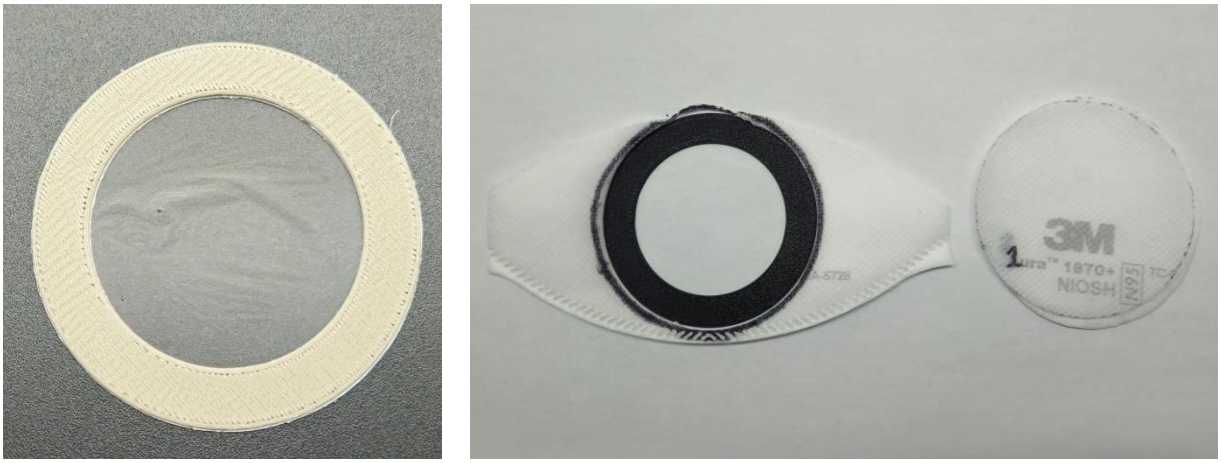

Figure 3-3 Nanofiber sample (left) and N95 (right) masks

3.3.2 Apparatus Setup

The apparatus ran at an airflow rate of 80 LPM for at least 1 minute before taking particle count measurements. Measurements were taken starting at the minute mark, starting with the upstream particle count followed by the downstream particle count. These measurements were repeated three times for statistical significance.

3.3.3 Filtration Efficiency & Pressure Drop

The filtration efficiency was presented as a histogram of the size of particles captured by the filter material. The calculation for efficiency is as follows. N_b corresponds to particles counted before, while N_a corresponds to particles counted after the filter material.

$$Capture\ Efficiency = \frac{N_B - N_A}{N_B}$$

The pressure drop is the differential pressure before and after the filter material. This difference was read directly from the test apparatus sensors.

3.3.4 Weight

The weight was presented as a single value per material. It was determined by weighting the filters before testing. The frame's weight was measured before and after mounting the fibers for nanofiber materials. The difference was determined to be the weight of the nanofiber material.

Chapter 4 Determination of Fiber Morphology

Summary: In this chapter, the effects of concentration, collector speed, solvent mix, and relative humidity were investigated, and the morphology of electrospun fibers in a sequential design of experiments was also explored.

4.1 Solution Concentrations

The morphological effects of solution concentration are directly proportional to the fiber diameter size and defects. The primary aim is to select a concentration that creates fibers produced with smooth and minimally defective surfaces for further experimentation. A secondary aim is to select a concentration that produces a density. This aim was determined through microscopy, as described in the design of experiments.

This study prepared PCL at three concentrations by weight in volume and Nylon at one concentration. Nylon characterization is extensive and well-understood, warranting minimal investigation [58]. PCL was prepared at 8%, 10%, and 20% in chloroform (CHL), while Nylon was prepared at 20% in Formic Acid (FA). The collector speed was fixed at 500 RPM, and the distance between the needle and drum collector was 20 cm. The behavior was characterized and used to select the concentration used in the following stages of the investigation.

Figure 4-1 shows that all concentrations produce smooth and defect-free PCL fibers. The material also exhibits alignment already in this study. The differences begin with the number of fibers produced and surface features present amongst the fibers.

The 8% concentration produces PCL fibers ranging from 250 nm to 10 µm. This range is large compared to the literature for PCL, which reports less than 2 µm [24]. The morphology of the

smaller fibers appears to be smooth, while larger ones exhibit a wrinkled appearance. Beading is present in the material between every couple of strands. The wrinkled feature is not ideal as a starting point for the following studies and will not be investigated further.

Increasing the concentration to 10% lowers the number of fibers produced. The strand size ranges from 104 nm to 5 µm, making it smaller than the 8% concentration. The surface morphology is consistently smooth, with no significant wrinkling present. Beading is present but not throughout the material, unlike the 8% concentration. This concentration produces smooth surface features with nanoscale fibers, which is ideal for investigating further.

At 12% concentration, PCL fibers decrease in quantity visually from the lower concentrations. The fiber size range is the smallest, from 373 nm up to 4.4 µm. However, wrinkled surfaces are prevalent in larger fibers. Like the 8% concentration, the wrinkled surface features are not ideal as a starting point for further investigations.

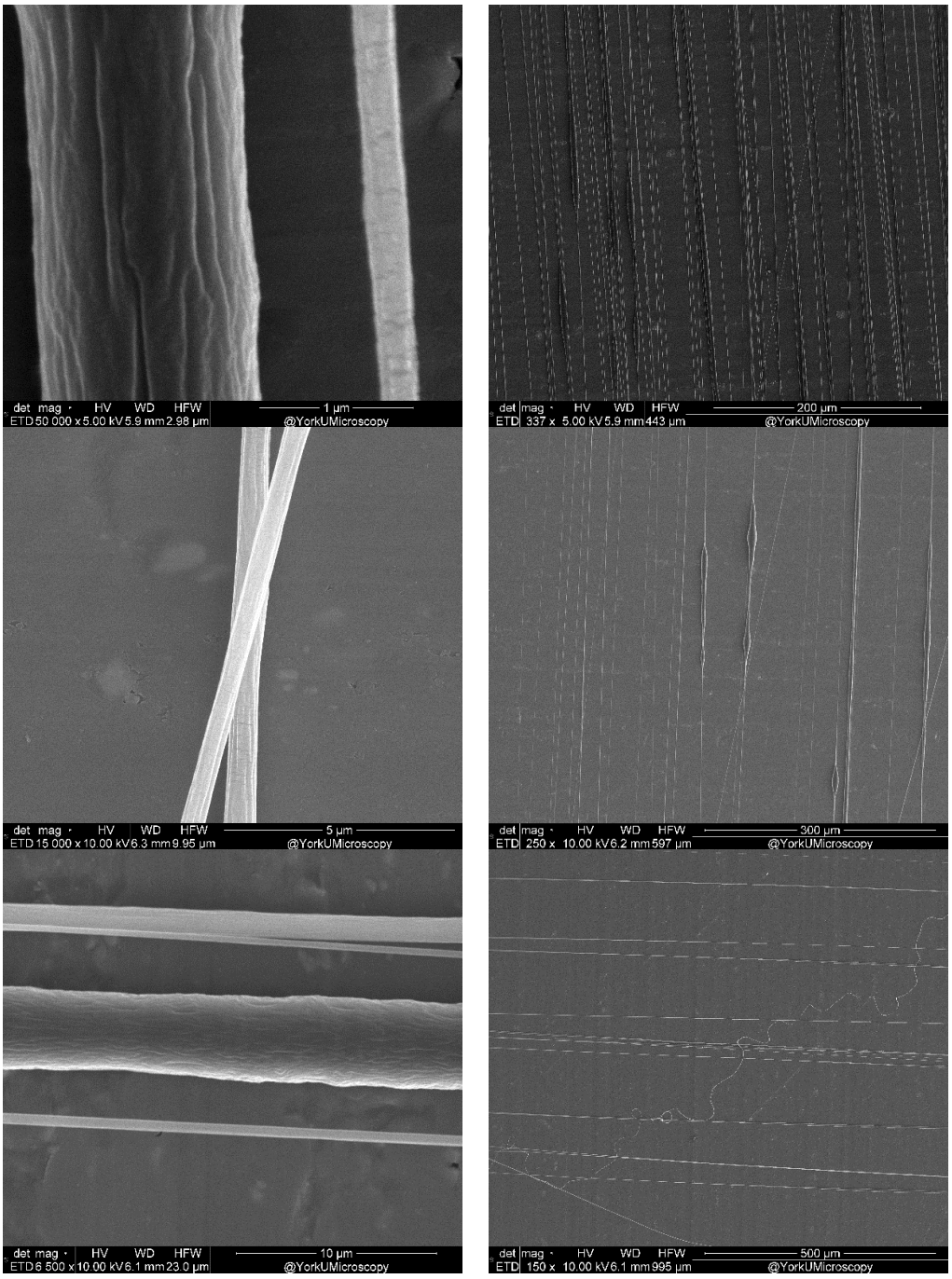

Figure 4-1 PCL fibers from concentrations of 8%, 10%, and 12% (top to bottom)

Nylon at 20% concentration produces smooth fibers with beading. The strands range from 25 to 256 nm, with a fiber quantity surpassing PCL at all concentrations. This concentration matches the

expected size for Nylon fibers at this concentration with minimal defects. The material exhibits no surface features, making this solution ideal for further studies.

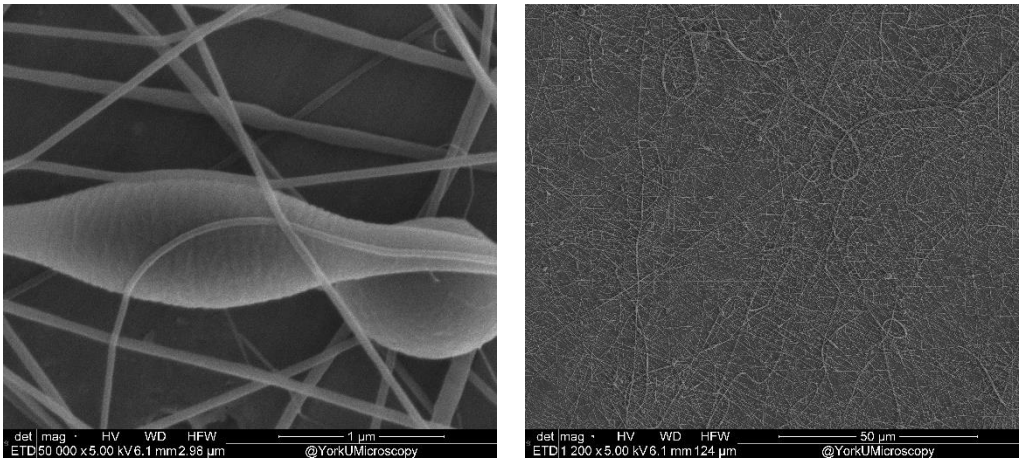

Figure 4-2 Close-up (left) of Nylon fibers from 20% concentration

4.2 Fiber Alignment

Fiber alignment depends on the collector speed in a drum collector. The increasing collector speed results in the increased alignment of fibers, leading to the stretching of the fibers. It was essential to run multiple speed steps to understand the transition point of randomly oriented fibers to aligned fibers in the material.

This investigation produced PCL fibers using a 10% concentration determined at the last stage and Nylon at 20%. Although alignment was already present in PCL, this study started at 100 to 500 RPM to study when the alignment was achieved. For Nylon, the collector speed ranged from 500 RPM to 2000 RPM. This data analysis gave us the collector speed necessary to produce randomly aligned fibers in the following studies.

10% PCL produces aligned fibers from 300 RPM up to 500 RPM. The aligned strands make the majority of fibers starting from 500 RPM. The distribution of aligned strands appears exponential.

The linear fibers start at 200 RPM up to 500 RPM. They make the majority of fibers at 300 RPM. The distribution of linear strands appears Gaussian. Random fiber frequency is present at all speeds from 100 to 500 RPM. The random strands make most fibers at 100 RPM up to 200 RPM. The distribution decreases exponentially with a temporary increase with the introduction of aligned fibers at 400 RPM. Since most fibers are aligned at 500 RPM, this is used for further studies.

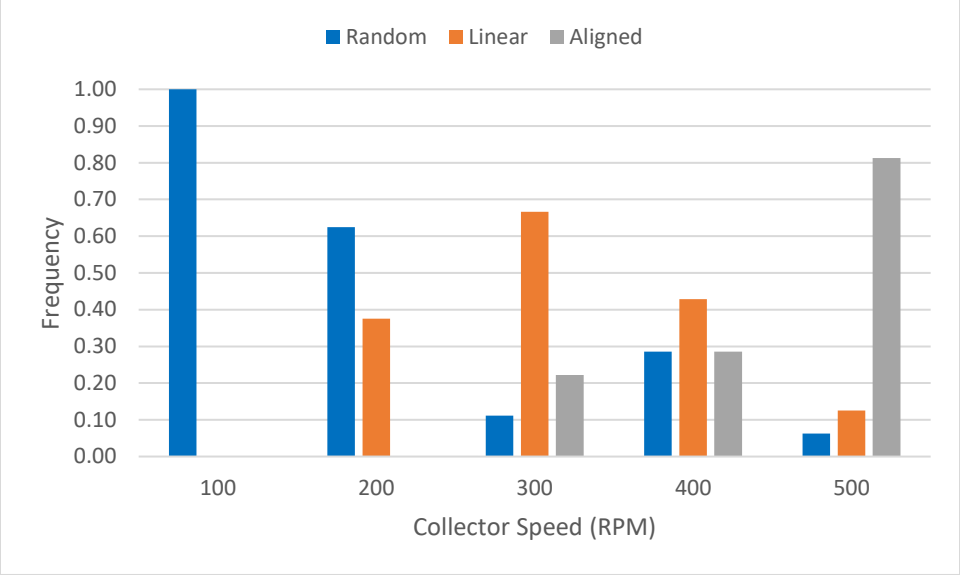

Figure 4-3 Fiber alignment frequency of 10% PCL solution

20% Nylon produces aligned fibers from 1000 RPM up to 2000 RPM. The aligned strands make the majority of fibers starting from 1800 RPM. The distribution of aligned strands appears exponential. The linear fibers exist at all speeds from 1000 RPM up to 2000 RPM. They make the majority of fibers from 1000 to 1600 RPM. The distribution of linear strands appears Gaussian. Random fiber frequency is present at all speeds from 1000 to 2000 RPM. The random strands remain the minority of strands at all speeds. The distribution does not seem to follow any trend precisely. The frequency of the random strands almost mirrors the aligned strands between 1200 and 1400 RPM.

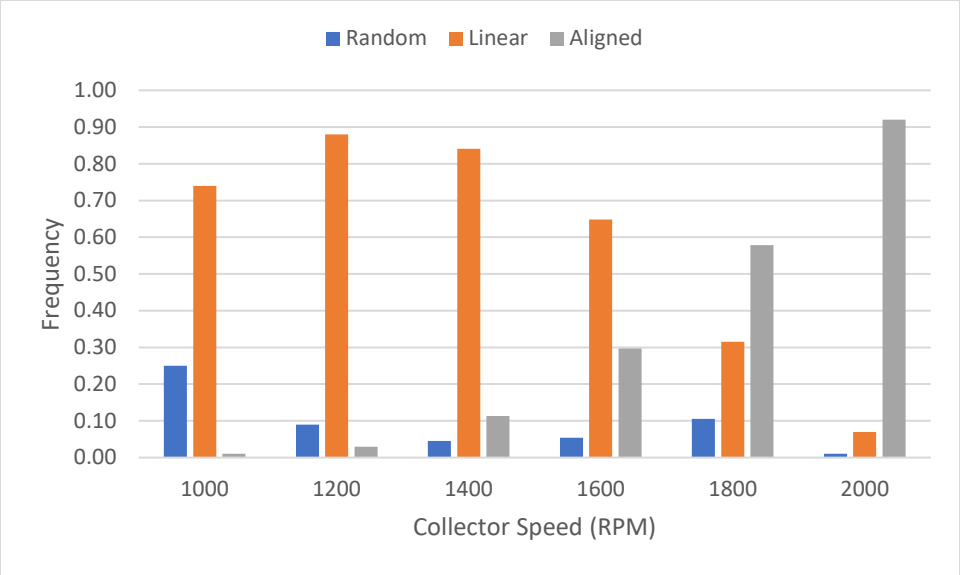

Figure 4-4 Fiber alignment frequency of 20% Nylon solution

PCL and Nylon exhibit similar behavior when producing aligned fibers by increasing collector speed. The trend is exponential for both with PCL exhibiting a majority of aligned fibers at 500 RPM and Nylon at 1800 and 2000 RPM. PCL did not exhibit fiber collection after 600 RPM while Nylon did but with no significant difference in result. Random strands trend on exponential loss for PCL, while Nylon is unclear.

4.3 Binary Solutions in Humidity

The morphological effects of humidity and solution ratio affect the fiber size and surface features. By varying the solution concentration and humidity levels, we can observe the impact of these two parameters on the fiber surfaces. This experimentation will help determine which parameter is more critical in creating featured fibers and to what extent. We investigated these effects using three humidity levels and three concentrations.

4.3.1 Polycaprolactone

The 10% concentration for PCL is remade with a secondary solvent, dimethyl formamide (DMF), in three ratios by parts 9:1, 8:2, and 7:3. Three relative humidities are used for testing at 25%, 50%, and 75%. The ratios 9:1, 8:2, and 7:3 are called first, second, and third concentrations for ease of reading. While for humidity, 25%, 50%, and 75% are referred to as low, medium and high humidity. All combinations except a solvent ratio of 7:3 at 75% humidity were tested, which produced no observable fibers. The favored combination was used to produce featured filter material for testing.

We were starting with the first and lowest concentration solution and low humidity. We observed fibers in the range of 279 nm to 2.23 μm. The smaller fibers were smooth and featureless, while the larger fibers appeared more wrinkled.

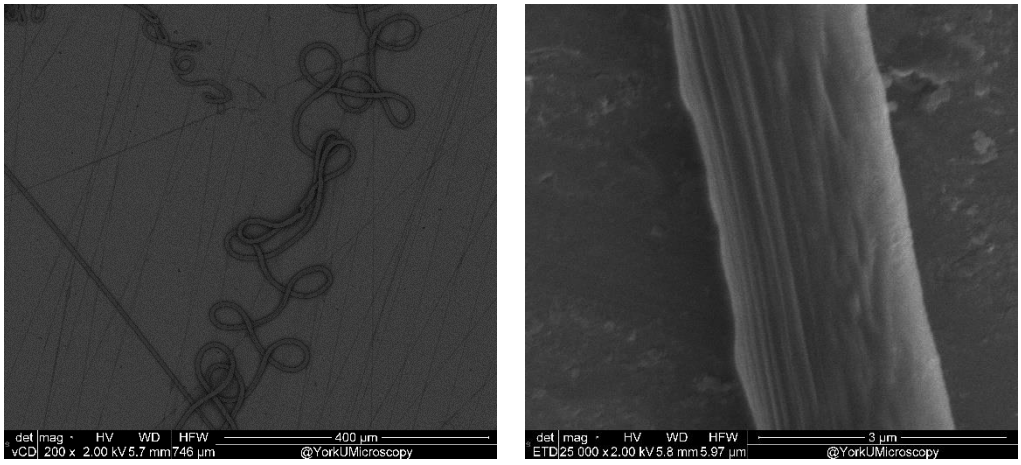

Figure 4-5 PCL 1:9 [DMF: CHL] 25% RH, fiber material (left) and largest (right) fiber

Looking at the first concentration solution and medium humidity, we observed fibers from 149 nm to 12.1 μm. The larger fibers showed signs of pitting, while the smaller fibers were smooth. The pitting appears to be developing larger features, which would indicate pores.

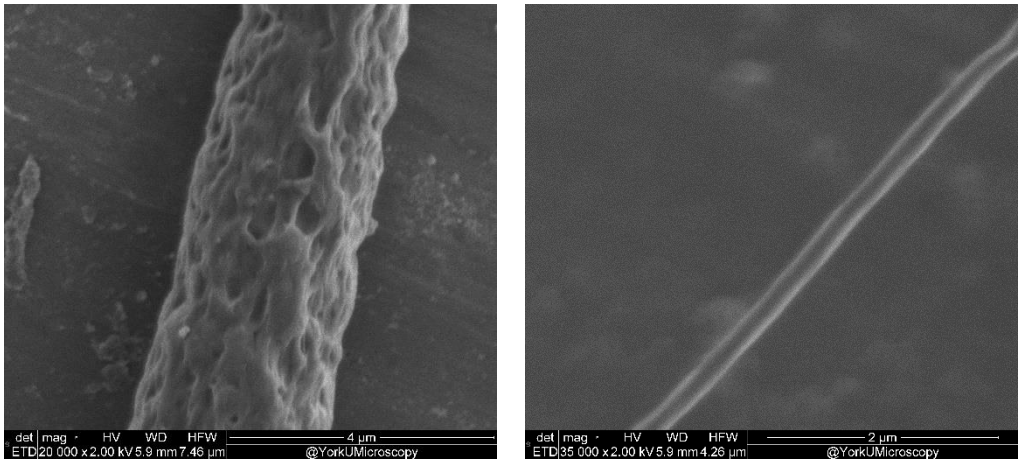

Figure 4-6 PCL 1:9 [DMF: CHL] 50% RH, largest (left) and smallest (right) fiber

The first concentration solution and high humidity produced only a few fibers. Their range was from 3.3 µm to 67 µm in size. The fibers are all porous but few in the total count. The pores show vast variation in size as well.

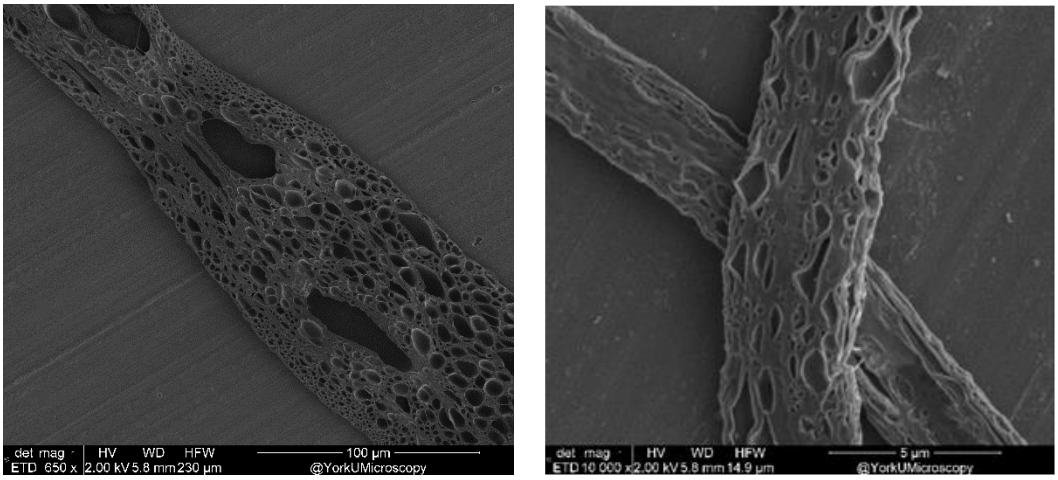

Figure 4-7 PCL 1:9 [DMF: CHL] 75% RH, largest (left) and smallest (right) fiber

Moving to the second concentration level at low humidity, we immediately observed the production of fibers from 73 nm to 2.6 µm. The surface morphology of these fibers appeared smooth and mostly featureless, occasionally exhibiting longitudinal ridges along their length.

Additionally, these fibers appeared well-aligned, likely due to the spinning speed aligning with PCL material properties.

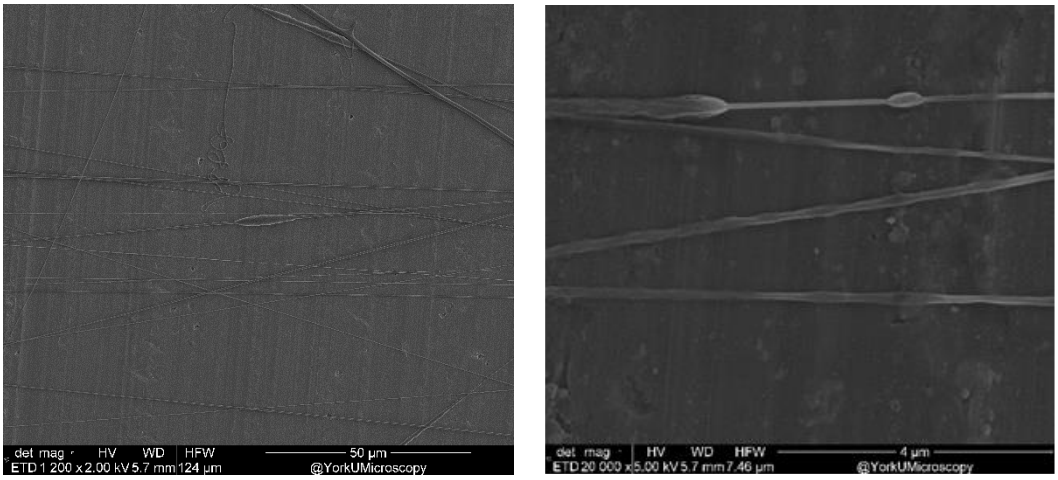

Figure 4-8 PCL 2:8 [DMF: CHL] 25% RH, fiber material (left) and smallest (right) fiber

At medium humidity with the second concentration level, we continued to observe aligned fibers; however, upon closer examination, the fibers did not appear smooth or cylindrical. The range of the strands were from 403nm to 10.9 µm. Increased humidity resulted in a pitted surface on the fibers. This effect was accompanied by contamination from the humidifier, manifesting as small particulates, assumed to be calcium deposits.

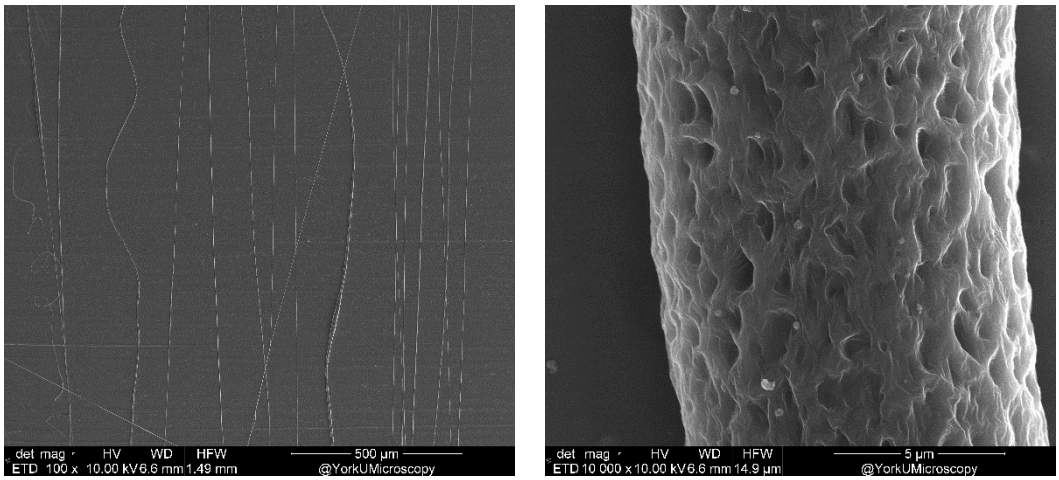

Figure 4-9 PCL 2:8 [DMF: CHL] 50% RH, fiber material (left), and surface morphology (right)

Lastly, a similar effect was observed at high humidity with the second concentration level, albeit with diminished surface features. The increased humidity caused the fibers to develop wrinkles, ranging in size from 405 nm to 3.62 µm. Despite these changes, the fibers remained in the nanoscale range, and the density of the fibrous collection persisted. The higher humidity induces a higher fiber production rate, possibly due to the increased electrical conductivity of the solution during the spinning process, allowing more material to be ejected into the spinning region.

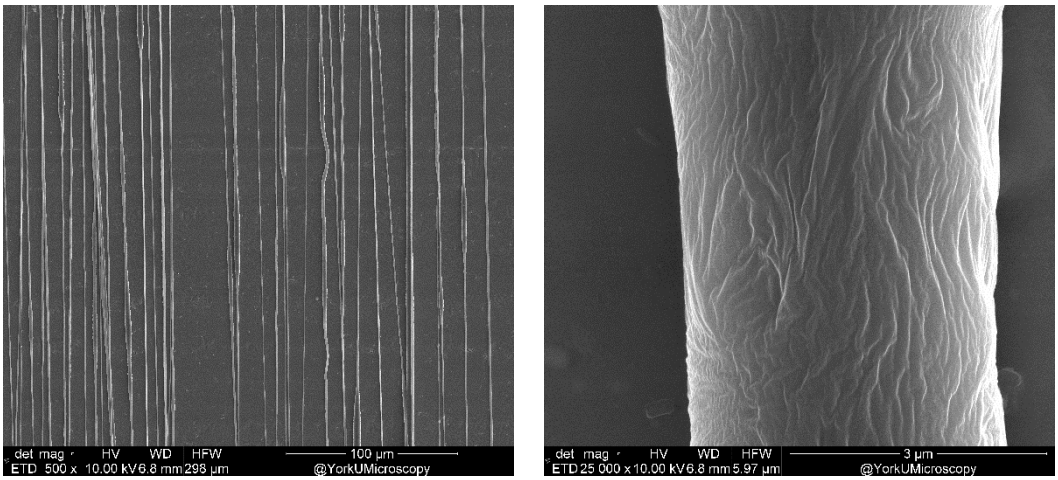

Figure 4-10 PCL 2:8 [DMF: CHL] 75% RH, fiber material (left), and surface morphology (right)

With low humidity, the third solution also produces a singular porous fiber changing in size between 4.5 µm and 7.63 µm. While the fiber appears highly porous internally, the solution humidity combination lacks adequate production for a testable material. Similar to the behavior observed in the first solution under higher humidity conditions.

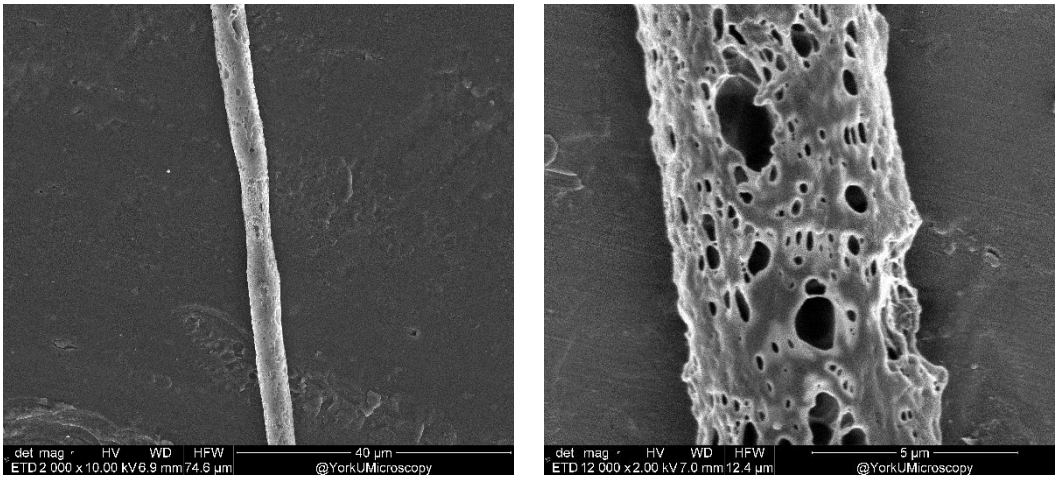

Figure 4-11 PCL 3:7 [DMF: CHL] 25% RH, porous fiber (left), and close-up (right)

We continue to observe similar behavior under medium humidity with the third solution but with a more significant presence of fibers. Smaller strands between 405 nm and 3 µm are produced.

The smallest fibers are featureless with smooth cylindrical surfaces, while the remaining exhibit wrinkled or porous surfaces. The quantity of fibers produced is small compared to the combinations tested at medium humidity.

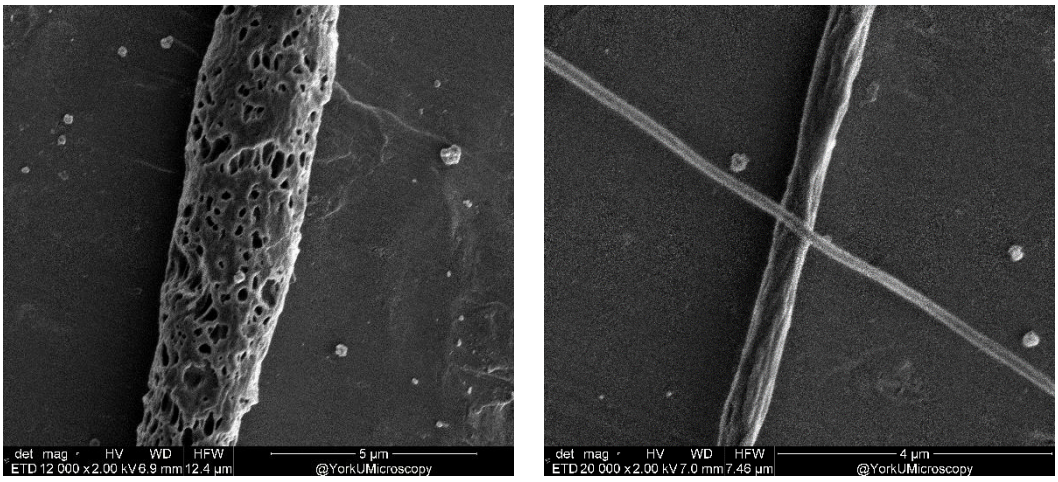

Figure 4-12 PCL 3:7 [DMF: CHL] 50% RH, porous fiber (left) and smallest (right) fiber size observed

PCL is a versatile material that can be diluted in multiple solvents and spun at various humidities to achieve featured surface effects. When humidity is low, not many surface features are achieved. Although with high humidity, you do see unique surfaces, the production rate of fibers is little or nonexistent. Medium humidity appears to be the best setting to produce fibers in any concentration. Additionally, between solutions at medium humidity, the first features rough pitted surfaces, the second a smooth pitted/porous surface, and the third wrinkled. We can select the second concentration at medium humidity as our candidate for producing porous nanofiber material for later testing.

4.3.2 Nylon

The 20% concentration for Nylon is remade with a secondary solvent, acetone (ACT) acting as the non solvent, in three ratios by parts 9:1, 8:2, and 7:3. Two relative humidities are used for testing at 50% and 75%. The ratios 9:1, 8:2, and 7:3 are called first, second, and third concentrations for ease of reading. While for humidity, 50% and 75% are referred to as medium and high humidity. All combinations were tested and produced fibers. The favored combination was used to produce featured fiber filter material for testing.

The first concentration at medium humidity produces smooth fibers. The strands range in size from 56 nm to 900 nm. The surface features are all smooth, featureless, and defect-free. Introducing acetone and humidity increases the fiber size range over double, with the largest strand being almost quadruple compared to the 20% Nylon baseline at 256 nm.

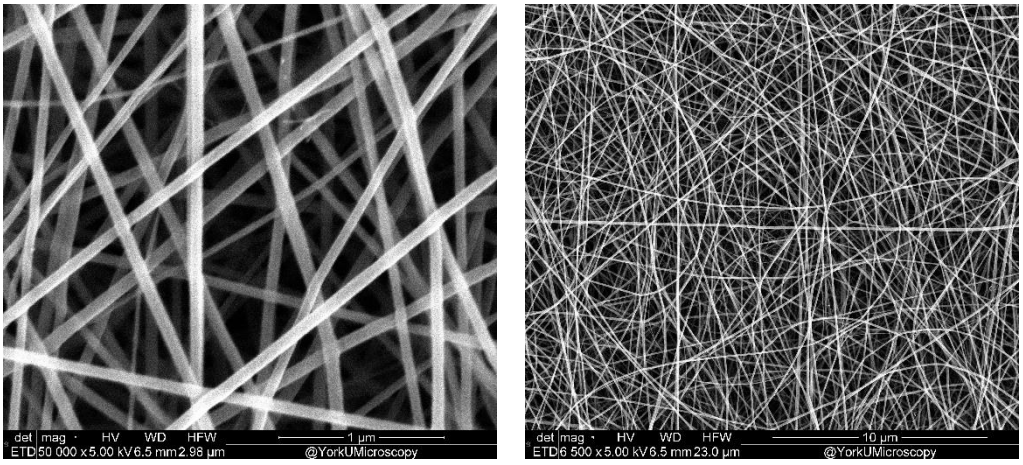

Figure 4-13 Nylon 9:1 [FA: ACT] 50% RH, close-up (left) and fiber material (right)

The second concentration at medium humidity produces smooth fibers, but beading has begun. The strands range in size from 48 nm to 198 nm. The surface features of all stands are smooth and featureless, with minimal beading defects. The defects occur only in the larger fibers. Increasing the secondary solvent has resulted in a smaller range than the 20% and first concentrations.

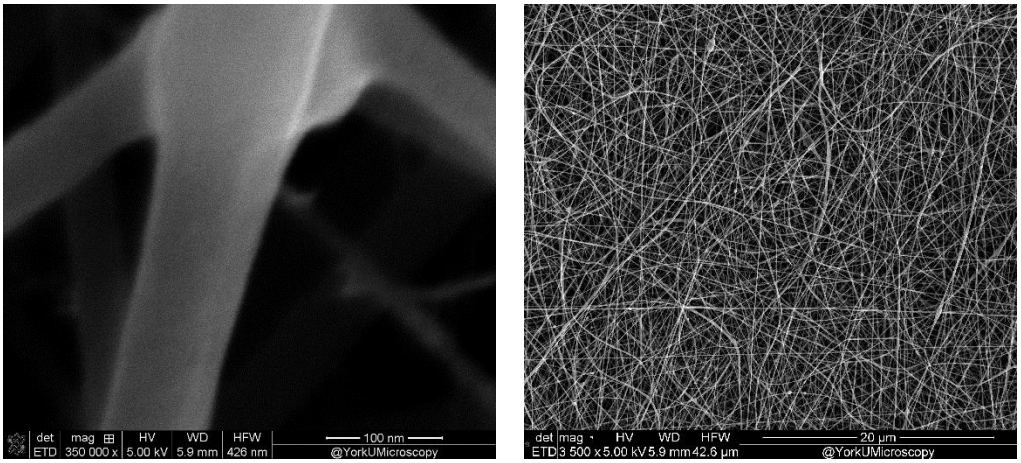

Figure 4-14 Nylon 8:2 [FA: ACT] 50% RH, close-up (left) and fiber material (right)

The third concentration with medium humidity produces mostly smooth fibers with the continuation of beading. The strands range in size from 60 nm to 357 nm, slightly increasing from the previous concentration but more than the original 20%. The beading is present amongst the larger fibers, an expected behavior for beaded defects. The third concentration does not produce surface features. In Figure 4-14, the production of nanonets is seen from the fiber material overview. The nets appear discontinuously through the material's span and appear similar in size to the surrounding fibers.

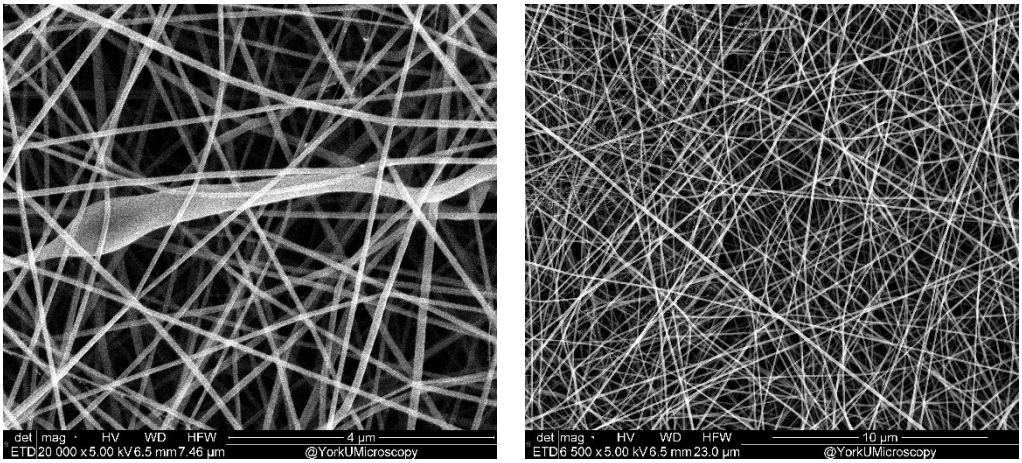

Figure 4-15 Nylon 7:3 [FA: ACT] 50% RH, close-up (left) and fiber material (right)

The first concentration at high humidity produces smooth but very beaded fibers. The range of strands begins from 45 nm to 900 nm. The beads exist throughout the entire size range of fibers. Additionally, the initiation of nano nets is evident in small pockets of fine fiber collections around larger strands. The formation is incomplete as it does not span many fibers.

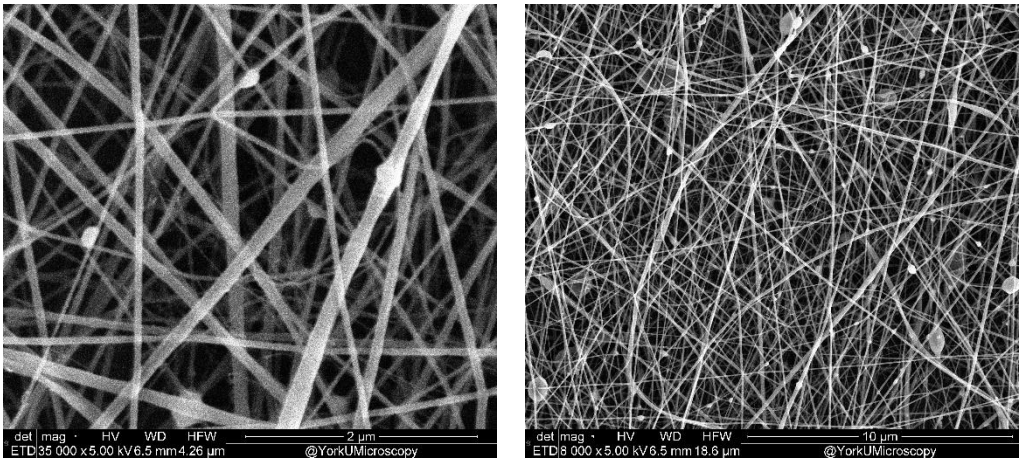

Figure 4-16 Nylon 9:1 [FA: ACT] 75% RH, close-up (left) and fiber material (right)

The second concentration at high humidity produces smooth and beaded fibers throughout the material. The range of strands begins from 45 nm to 156 nm. This range does not change much

with the increase in humidity. There are no notable surface features among the fibers in this material.

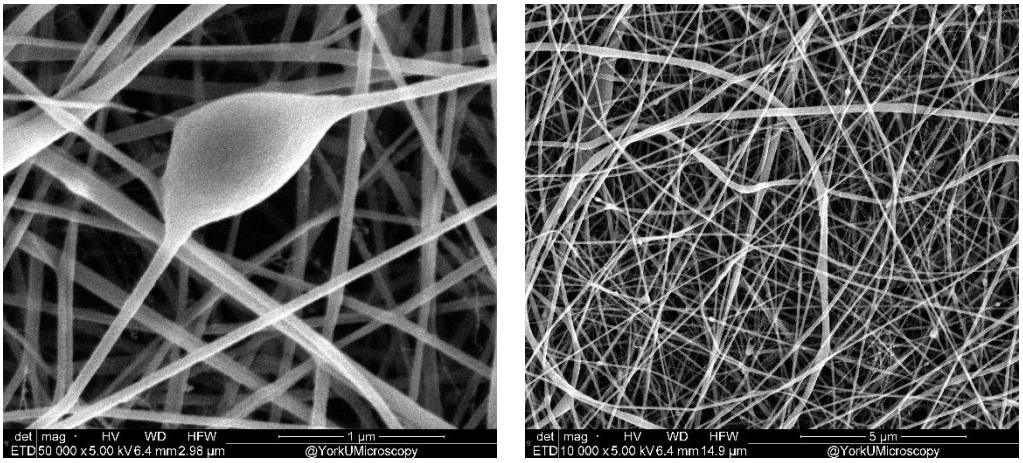

Figure 4-17 Nylon 8:2 [FA: ACT] 75% RH, close-up (left) and fiber material (right)

The third concentration at high humidity produces smooth fibers with reduced beads compared to the previous concentration. The range of fibers begins from 40 nm to 300 nm, not significantly different from the medium humidity result. There are surface features in this concentration and humidity but on the beads, not fibers.

Some trends observed through this study show a relationship between beading and solvent ratio or humidity. Increasing either parameter leads to a high beading production, particularly with the changing humidity. The range of fiber sizes does not significantly change between humidities; however, an increase in secondary solvents reduces the range of fibers produced when comparing solvent ratios.

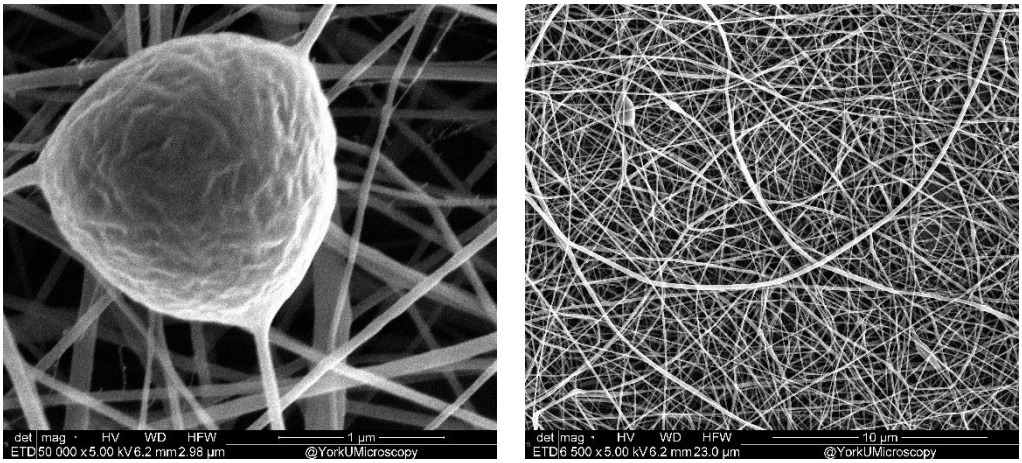

Figure 4-18 Nylon 7:3 [FA: ACT] 75% RH, close-up (left) and fiber material (right)

Chapter 5 Development of Material Performance Test

Summary: In this chapter, we discuss the design methodology of the aerosol testing apparatus. We observed operational limits and behavior of particle generation and air stream velocity.

5.1 Apparatus Design

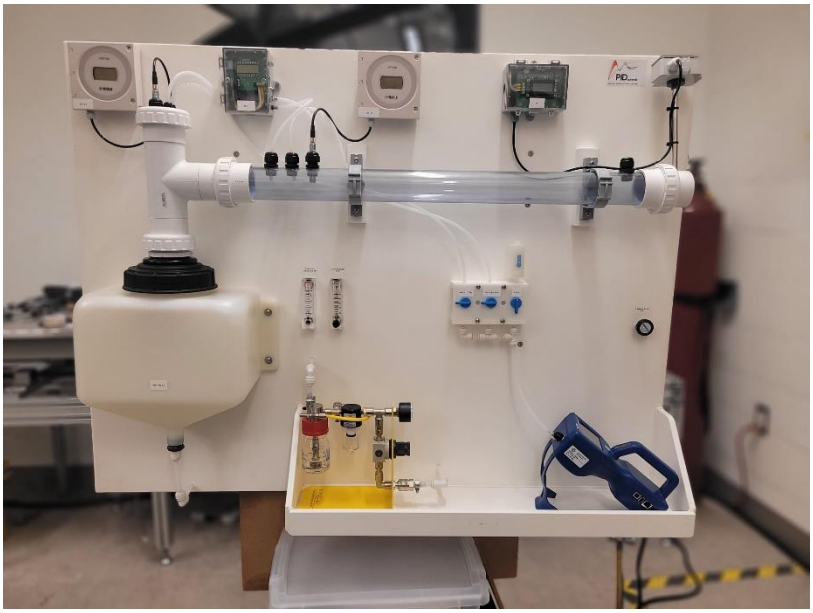

Figure 5-1 Assembled test apparatus overview

The design for the testing apparatus followed the schematic presented in the methodology. It consists of a particle generator, conditioning units, an inline sample mount, and sensors for instrumentation. The design was based on the air supply, measured at 5.5 bar with a flow rate of 100 liters per minute (LPM). This was then used to determine the appropriate sample size for the target ASTM face velocity.

Preconditioning

The air was minimally conditioned as it was already extremely dry, and determined not to need an inline dryer or nebulizer. The flow was split and run in parallel to a particle generator (Topas ATM

221), as can be seen in Figure 5-1 in the yellow at the bottom shelf of the setup. The air was then merged and sent into a buffer tank before reaching the sample holder.

Figure 5-2 Buffer zone including the filter test stage with sensors before and after

Sampling

The setup collects data using temperature, humidity, and pressure sensors before and after the setup. Particle count was taken on counter (TSI 9306-03) connected in line with other sensors. The samples were mounted directly onto a PVC pipe compression fitting. The size of the pipes was selected to be a 2 in internal diameter to allow the flow to hit both 80 LPM and also achieve air velocities of 0.5 to 25 cm/s at the filter material.

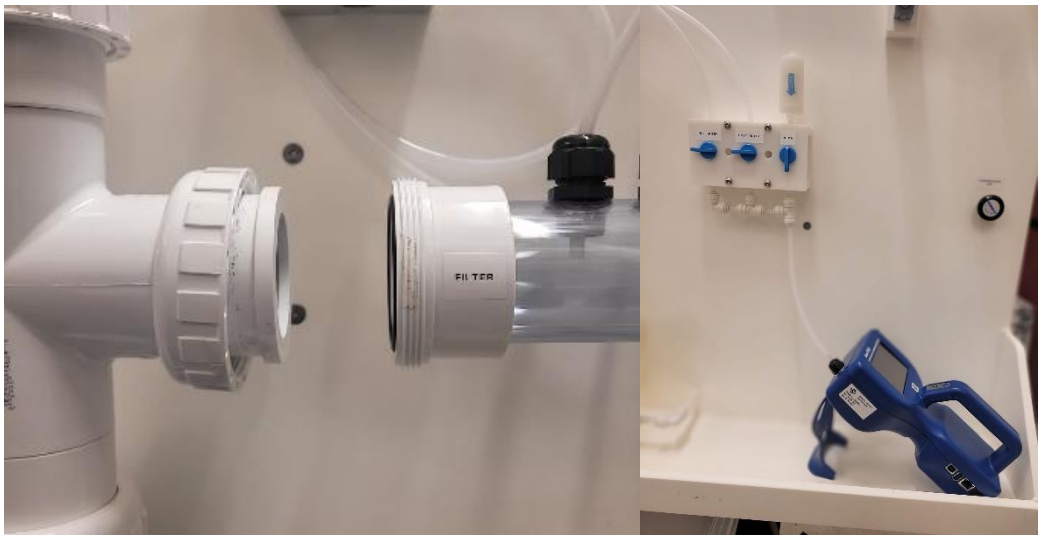

Figure 5-3 Compression fitting for filter mount and particle counter with sampling tubes

Post Processing

Two streams of data were collected for this system from the particle counter and the test apparatus controller located at the back of the setup. The data from the particle counter was collected by USB and manually processed on Microsoft Excel. Flow rate and face velocity were determined through a localized control panel software via ethernet, logging everything into a local SQL server.

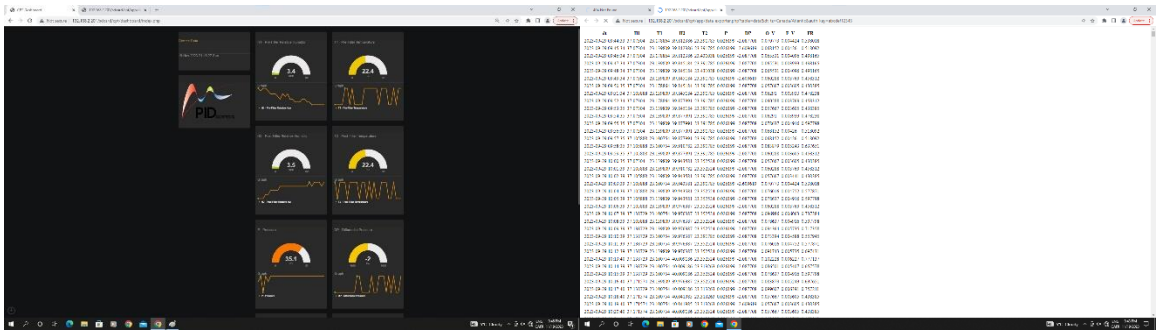

Figure 5-4 The localized control panel software and SQL server log

5.2 Particle Distributions

The test apparatus was run at a fixed flow rate while varying the input diverted to the particle generator. The aim here was to investigate the effect on the particle distribution generated. Di-

Ethyl-Hexyl-Sebacat (DEHS) was used as the salt for generating the particles, a common material in clean room and filter testing. DEHS was used instead of latex and sodium chloride, two commonly used materials in standards, however safety was taken into consideration since the apparatus was open to atmosphere. This also allowed us to compare our results with the calibration provided by the factory which was done with DEHS. The particles generated by the system range from 0.1 µm to 1 µm in size. In comparison, our particle counter captures a range of 0.3 µm to 5 µm.

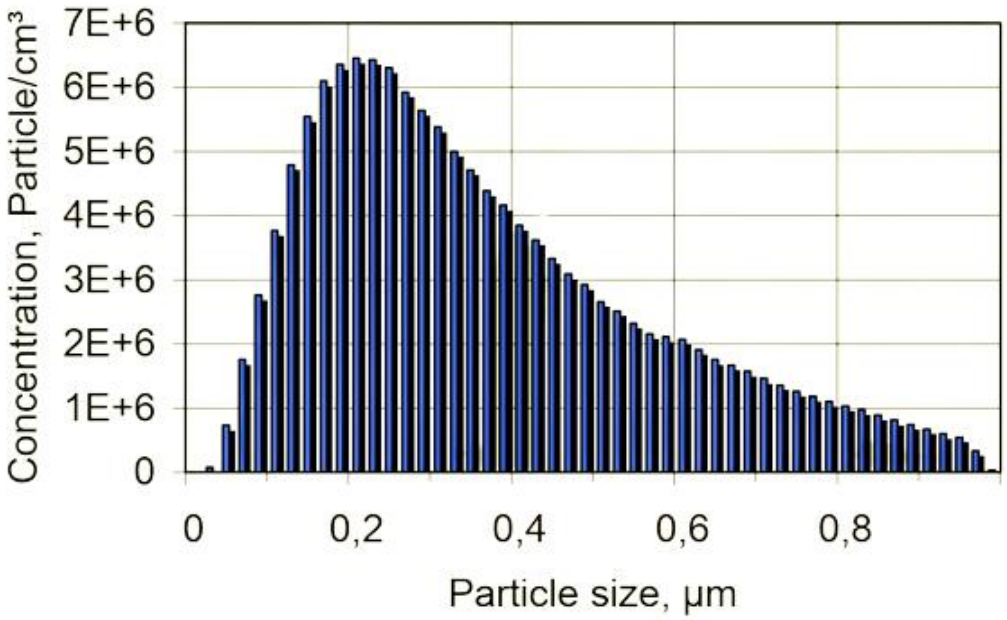

Figure 5-5 Particle size distribution for DEHS aerosol measured with particle sizer (reproduced from manufacturer's data sheets)

The particle counter has built-in functionality for detecting coincidences, a phenomenon when a group of smaller particles get counted as a larger particle, in the form of a laser scatter warning. The testing apparatus flow rate ran at 80, 50, and 30 LPM. The particle generator ran at 0.5, 0.75, and 1 bar at each flow rate. Figure 5-6 presents the only observable particle distributions captured

by the system. The particle generation in all other combinations produced more particles than the counter could operate with. Thus, a limitation in our system was identified. The particle distribution at 0.75 bar did not resemble the trend produced by the manufacturer. The distribution decayed logarithmically, whereas the manufacturers followed exponent loss. The 0.5 bar distribution, in comparison, was significantly lower in particle count but followed the manufacturer's trend of an exponential loss. The particle counter displayed a laser scatter warning, which meant the particle distribution could not confidently be measured due to coincidence. A phenomenon where smaller particles count toward a bigger particle. Thus, 0.5 bar was selected as the operational default for producing aerosol in the test apparatus.

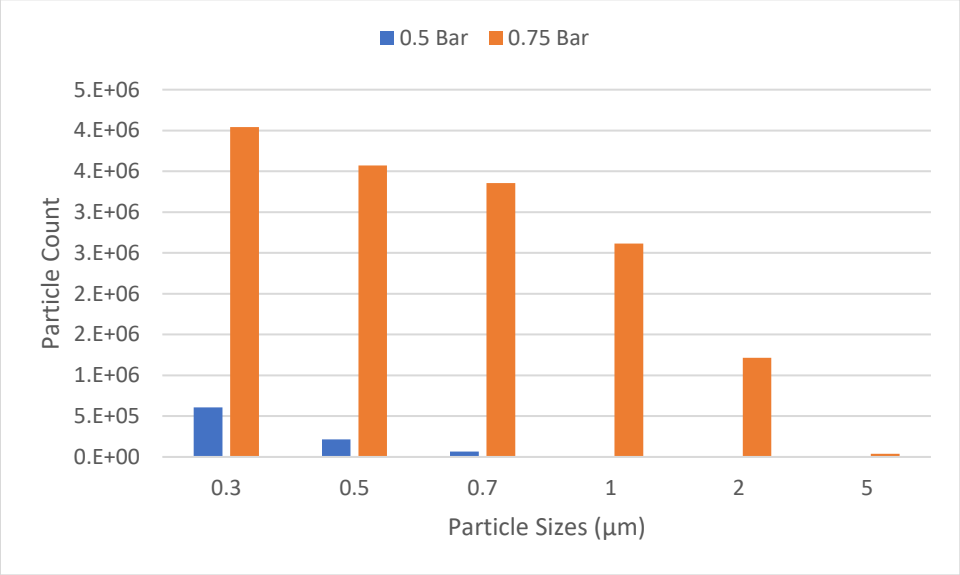

Figure 5-6 Particle size distribution for DEHS with TSI particle counter at 80 LPM

5.3 Sample Preparation

The thickness of nanofiber materials makes it difficult to manipulate to create testable samples. The process involved removing nanofibers from an aluminum foil substrate and securing it onto a frame. The separation was initially conducted with a water bath.

The challenge became apparent after detaching from the substrate. Attachment proved difficult as the fibers remained delicate in the water and impossible to grip. When gripped, the material was likely to rip. An alternative was attempted in which the test frame was mounted onto the fiber material prior to dipping with double-sided tape. The result was a nanofiber material mounted onto a round frame suitable for testing. Other mounted methods such as metallic meshes for the substrate were considered but dismissed due the difficulty in mounting and unmounting from the drum collector.

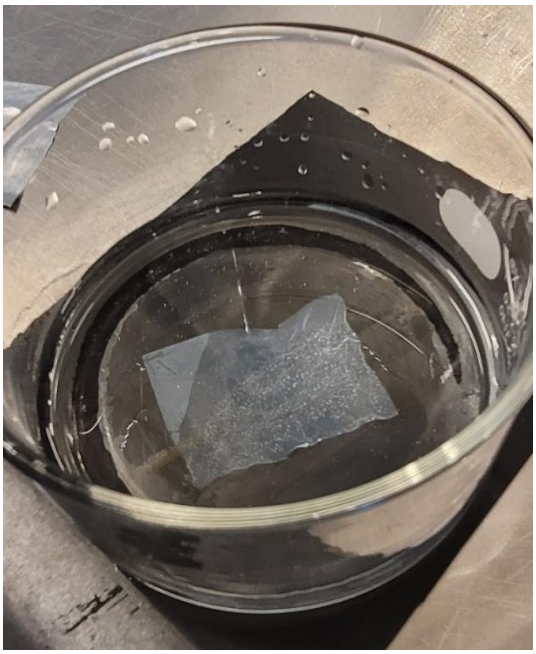

Figure 5-7 Detached fibers in a water bath

Figure 5-8 Torn nanofiber material mounted on plastic frame

The fiber side of the frame was faced towards the exhaust of the setup due to the reduced contact created by a rubber o ring. This reduction aided in mounting and dismounting the nanofiber specimens, as the double-sided tape was still effective through the material, causing sample sticking.

Figure 5-9 Mounted nanofiber frame in test apparatus

Chapter 6 Evaluation of Filter Materials

Summary: In this chapter, the performance of surgical and commercial masks is presented. The layers of the masks are also studied individually to understand their role in mask performance. The electrospun masks developed in this research are tested standalone and as a hybrid layer of a surgical mask.

6.1 Surgical Masks

This study prepared surgical and commercial N95 masks as a whole and in individual layers. They were tested in the aerosol tester running at 80 LPM and standard particle generation. Their behavior was characterized to understand the performance of the individual layers separately and together. This behavior acted as a baseline for the fibers developed in the previous study to compare performance.

The filtration efficiency of the surgical mask provides complete capture efficiency for particles 5 µm and above. However, this efficiency declines below this range. The surgical mask has a noticeable dip in capture efficiency when moving to submicron particles. When looking at the individual layers of the surgical mask, we observe that the first and third layers do not provide significant filtration efficiency, as the second layer does the bulk of the filtering. This behavior matches the indicated design of surgical masks. We noticed marginal differences in the second layer, and mask performance is at 0.3 and 5 µm, which suggests the first and second layers impact overall performance. This performance is evident with the first layer aiding in the bulk filtration of 5 µm particles. In contrast, there is a 5% difference in the second layer and overall mask performance.

The pressure drop for the surgical mask presents a similar trend. The pressure drop of individual layers appears to be relatively cumulative, with the first and third layers exhibiting roughly 20 pascals and the second layer with 170. This drop is close to the overall pressure drop of 205 observed for the total mask.

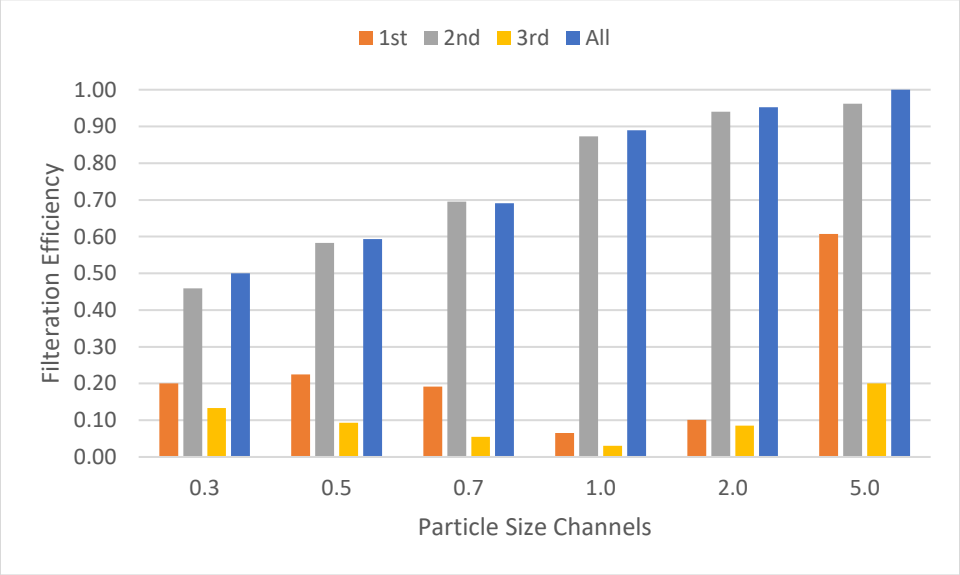

Figure 6-1 Filtration Efficiency Commercial Mask with Layer Breakdown

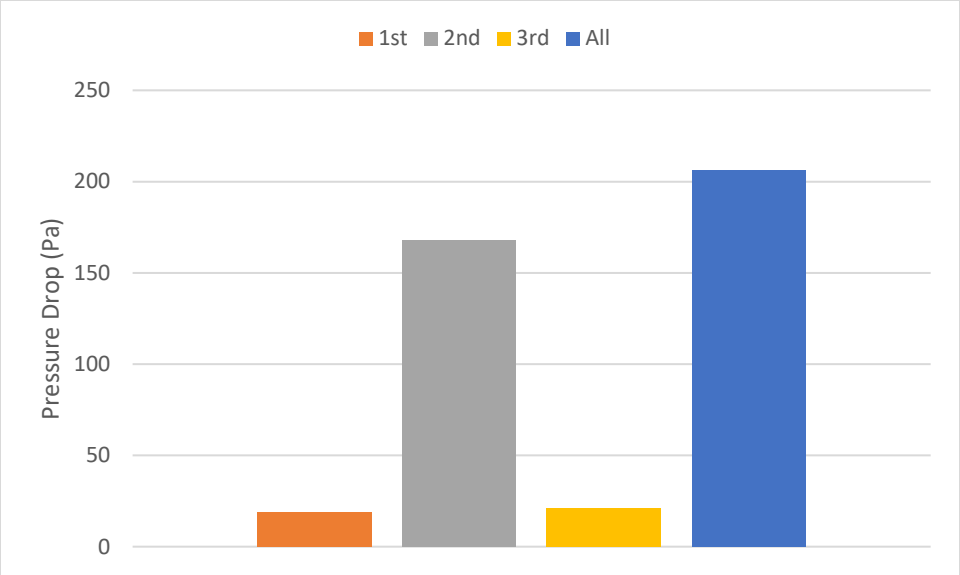

Figure 6-2 Pressure drop of a commercial mask with layer breakdown

6.2 Commercial Masks

The performance of the N95 mask exceeds the expectation of its rating. The mask collectively filters all observable particle sizes with an efficiency of 99% or more. When observing the individual layers, it becomes evident that the first and second layers are not primarily filtering layers, and the third layer holds the bulk of the filtration capabilities. We noticed filtration performance from the first and second layers above the micron range between particles sized one to five µm. The first layer shows good filtration efficiency for particle sizes of five µm and consistently outperforms the second layer by almost double efficiency. However, we observed that the second layer matches the performance of the first layer in this submicron range.

The pressure drop of the overall mask is an astounding 400 pascals, double that of the surgical mask. Similar to the first and third layers of the surgical mask, the commercial masks' first and second layers appear to have minimal pressure drop. The bulk of the pressure drop exists in the third layer, which also holds the most filtering capabilities. The cumulative pressure drop of the layers is not exact but appears somewhat equivalent to the overall mask.

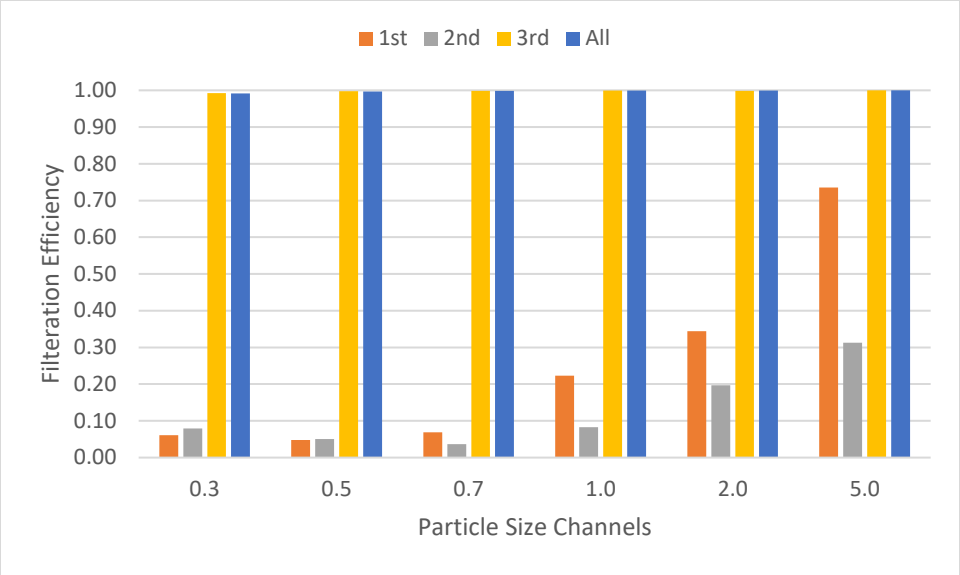

Figure 6-3 Filtration efficiency of N95 mask with layer breakdown

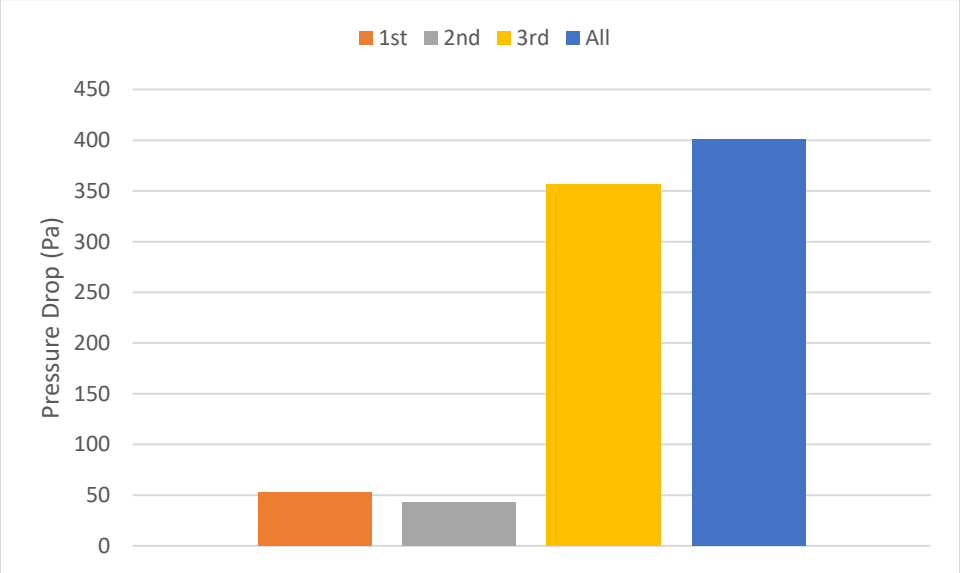

Figure 6-4 Pressure drop of N95 mask with layer breakdown

6.3 Electrospun Masks

This study prepares electrospun fibers of a solid random solid aligned and porous aligned nature. The electrospun filter material is tested individually and as an embedded layer in a surgical mask. We investigate the ability of the developed material to act as a standalone or support material. Additionally, we compare the performance of the different fiber materials. The material studied in the following sections is PCL.

6.3.1 Solid Random Fibers

The filtration efficiency of the randomly aligned fibers appears to follow the same trend as the surgical mask; however, it falls short consistently by at least 10%. When the fibers substituted with the original filtering layer in a surgical mask, the performance marginally improves by 2 to 3%. Nevertheless, we noticed a drop in performance when capturing particles sized 5 μm. The standalone pressure drop of the randomly aligned fibers is lower than the hybrid surgical and commercial. This drop is ideal for prolonged use since it is lower than the current surgical and N95 masks.

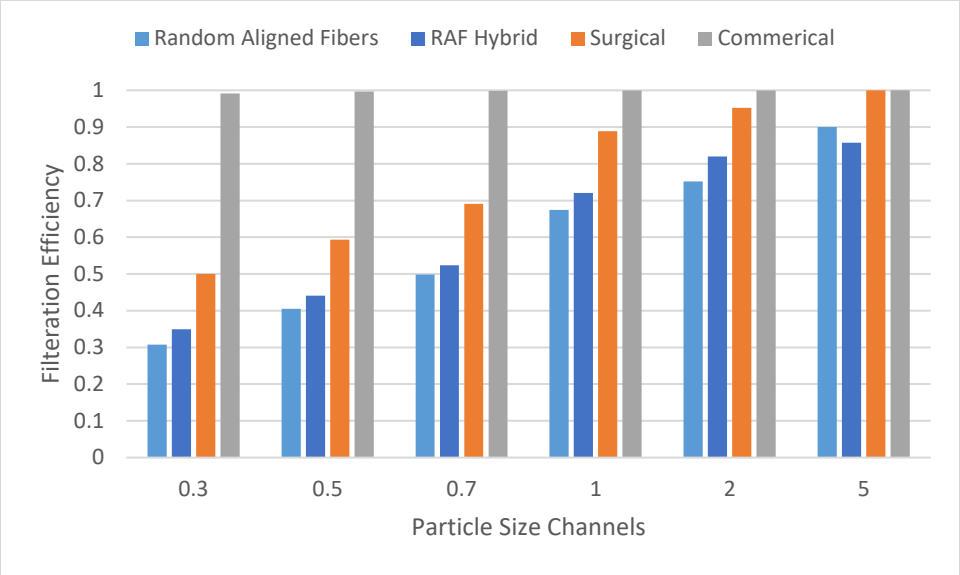

Figure 6-5 Efficiency of randomly aligned fibers in contrast to surgical and commercial

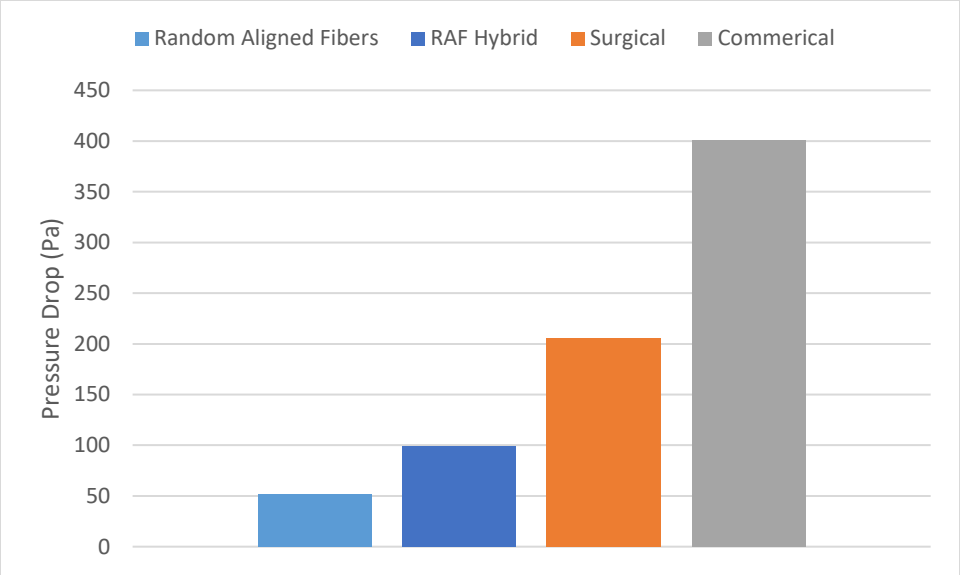

Figure 6-6 Pressure drop of randomly aligned fibers in contrast to surgical and commercial

6.3.2 Solid Aligned Fibers

The filtration efficiency of solid aligned fibers appears to follow a similar trend to surgical masks. It consistently falls short by a smaller margin of 5% on average. When embedded in a surgical mask, the performance does not improve. Rather, we noticed a dip in performance consistently in all particle sizes except two µm. The pressure drop also appears low, with the standalone exhibiting roughly 100 Pa and the embedded aligned fibers exhibiting 140 Pa. This drop is better than the surgical and commercial masks that sit around 200 and 400 Pa.

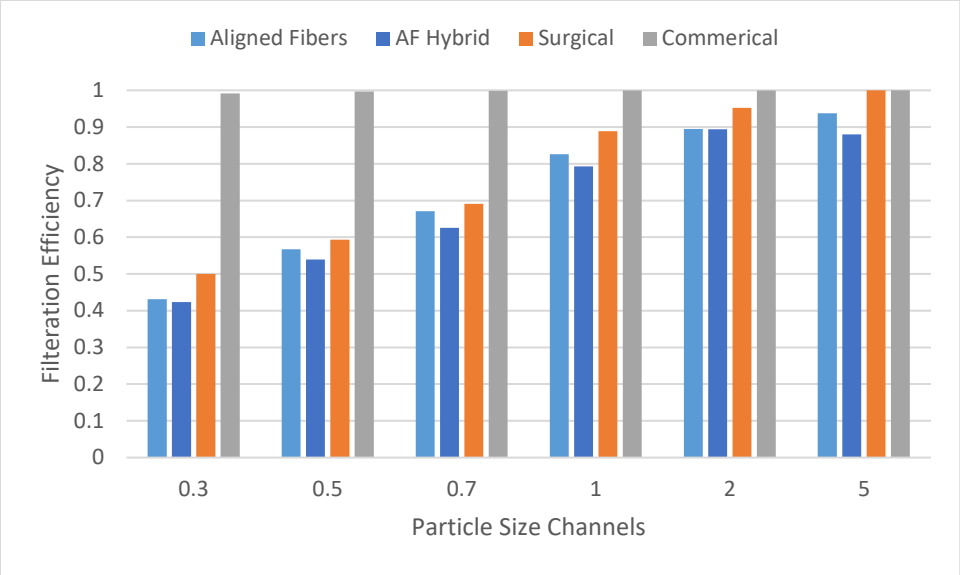

Figure 6-7 Filtration efficiency of aligned solid nanofiber materials

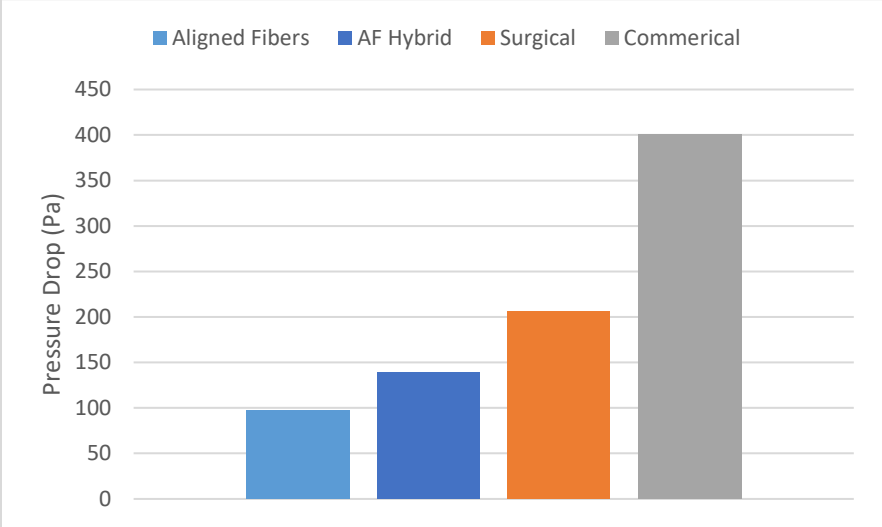

Figure 6-8 Pressure drop of aligned fibers in contrast to surgical and commercial

6.3.3 Porous Aligned Fibers

The filter efficiency of porous aligned fibers appears to follow an exponential trend but does not resemble the surgical or commercial mask. It consistently performs below the efficiency of a

surgical mask by at least 40% at any given particle size. Embedding the porous aligned fibers improves the performance of the hybrid surgical mask compared to the standalone porous aligned fibers. Still, it falls short of the surgical mask performance. It follows a similar trend to the standalone porous aligned fibers exhibiting 2 to 5% improvement for particle size of 0.3 up to 5 µm.

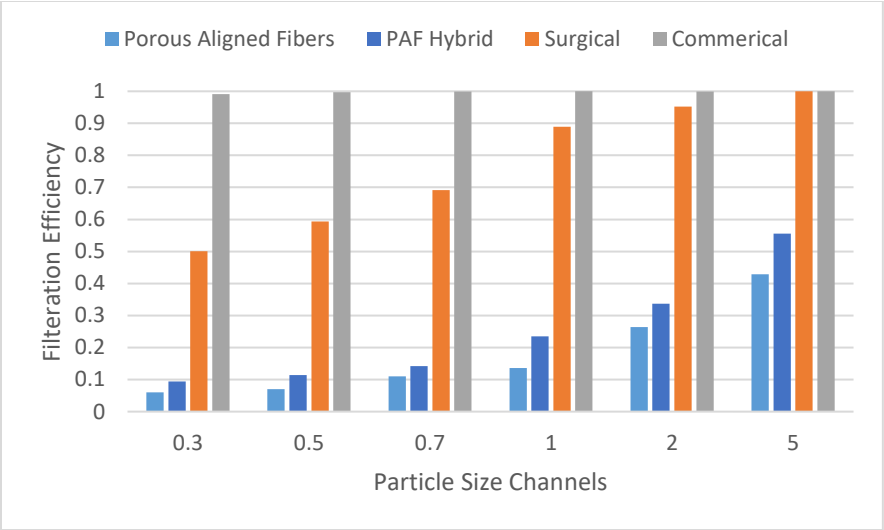

Figure 6-9 Particle filtration efficiency of single-layer aligned porous fiber coupon

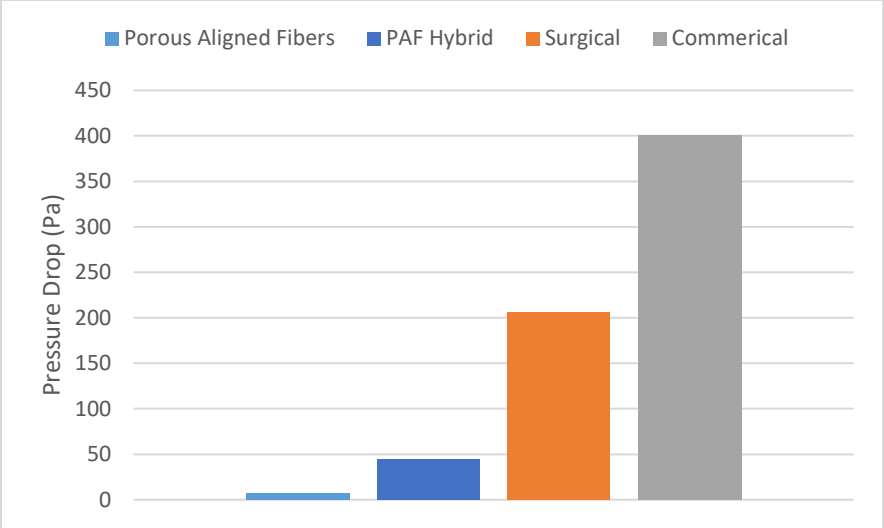

Figure 6-10 Pressure drop of porous aligned fibers in contrast to surgical and commercial

A trend is not apparent when comparing porous aligned, aligned, and random fiber materials. While the aligned fibers offer better filtration efficiency than the random variant, the porous aligned perform poorly in efficiency and have a low-pressure drop. This behavior can not be attributed to the surface features of the fibers alone. Thus, another parameter that needs to be investigated is weight.

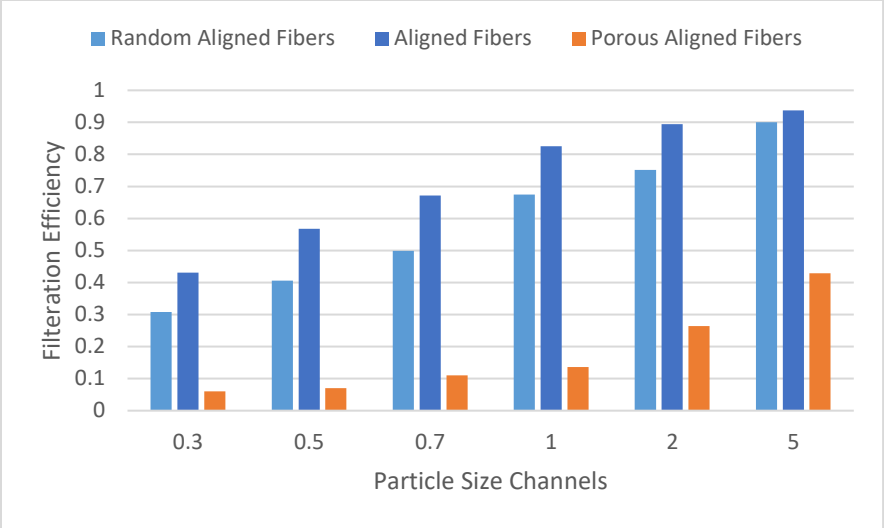

Figure 6-11 Particle filtration efficiency of random vs. aligned vs. porous aligned fibers

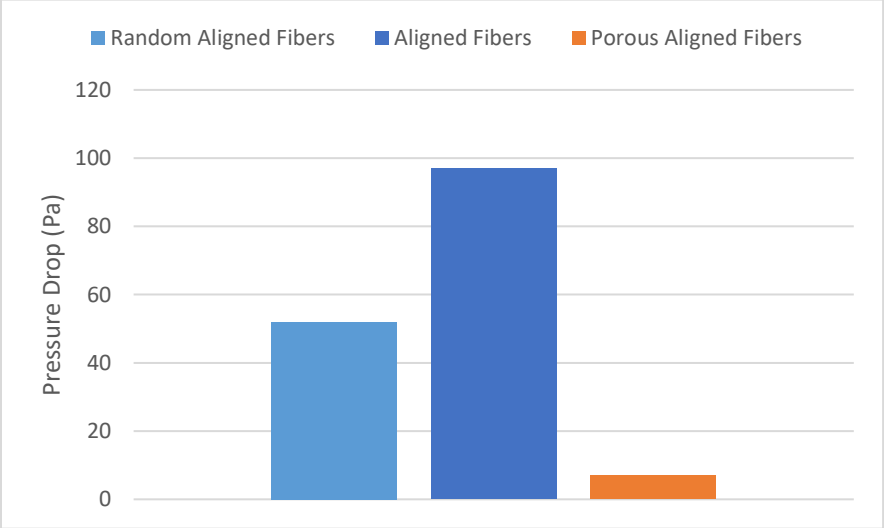

Figure 6-12 Pressure drop of random vs. aligned vs. porous aligned fibers

6.3.4 Weight

This study presents the weight of electrospun fibers to explain their behavior. PCL fibers of a solid random solid aligned and porous aligned were investigated. The samples used for measurement were the same samples used in mounting filters in the tester. The electrospun filter material is tested individually and as an embedded layer in a surgical mask. We investigate the ability of the

developed material to act as a standalone or support material. Additionally, we compare the performance of the different fiber materials. The material studied in the following sections is PCL.

The weight of the PCL fibers in random, aligned, and porous aligned configurations provides insight into the amount of material working in each mask. Figure 6-13 suggests similar amounts of material are produced in the random and porous align PCL filter. This similarity makes it easy to compare the results. PCL random fibers consistently perform over double the efficiency of porous aligned fibers. However, they hold an inferior pressure drop of 52 Pa compared to 7 Pa. The difference between random and aligned seems to follow the trend in their weights. Filters with aligned strands have a filtration efficiency, pressure drop, and weight 1.5 times that of randomly aligned strands. This linear trend suggests no significant performance improvement is achieved by aligning the fibers. Rather, porous fibers appear to be where the focus should be.

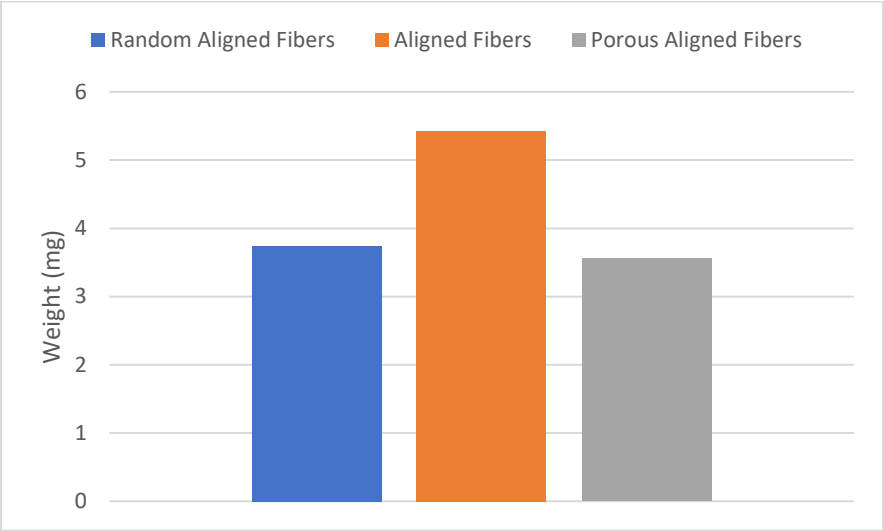

Figure 6-13 Weight of PCL nanofibers

6.3.5 Nylon Fibers

The Nylon fibers produced material that exceeds the capabilities of the test apparatus used in this work. The pressure drop exceeded the sensor threshold at 1000 Pa, and the filtration efficiency

was no less than 100% at all particle ranges. However, the flow rate over the material was close to zero, suggesting the material is not acting like a filter but rather like a solid material, rendering the material useless for filtration applications. Regardless, the weight of Nylon combinations was taken.

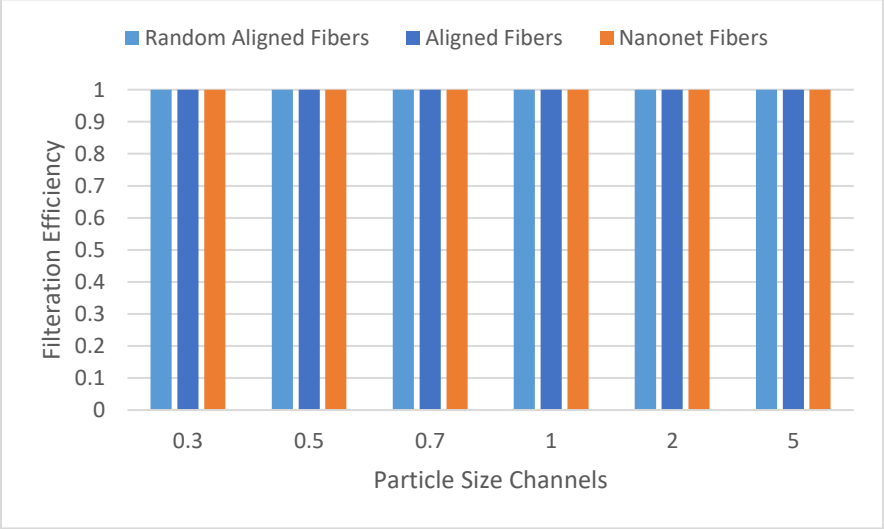

Figure 6-14 Particle filtration efficiency of random vs. aligned vs. nanonet Nylon fibers

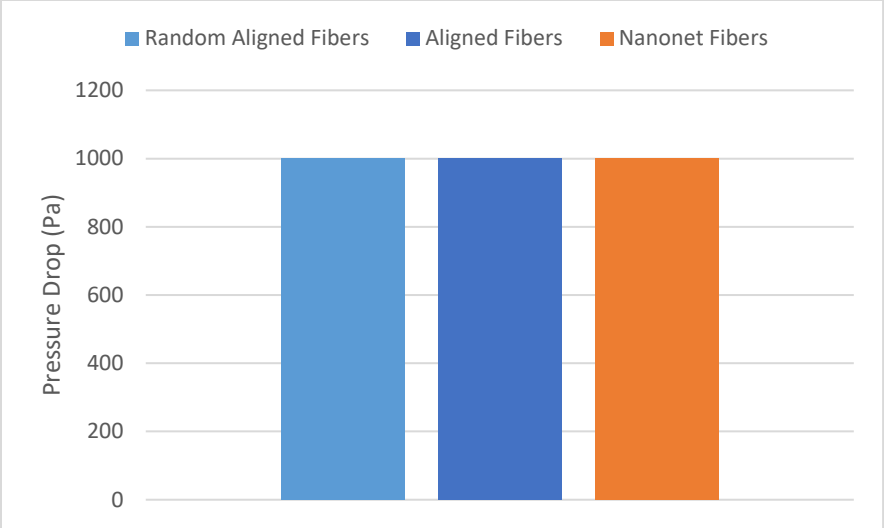

Figure 6-15 Pressure drop of random vs. aligned vs. nanonet Nylon fibers

Like PCL, the aligned fiber weights in more than the random strands. However, the nanonets present in the Nylon make the sample weight triple, unlike the porous fibers in PCL. This difference would agree with literature suggesting humidity caused the material to eject rapidly, leading to more material captured.

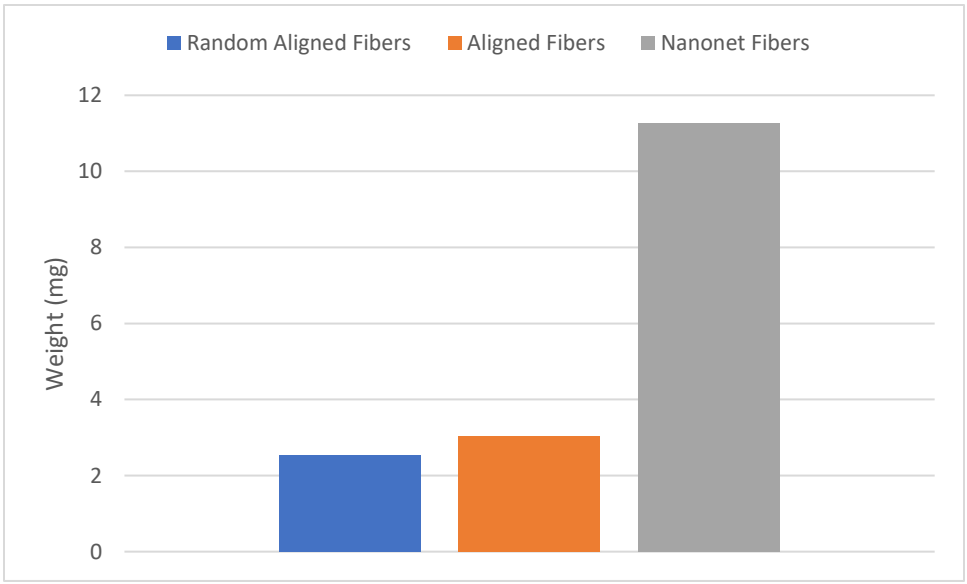

Figure 6-16 Weight of Nylon nanofibers

Chapter 7 Conclusion

Summary: In this chapter, the problem statement is restated, the research objectives are summarized, and contributions from this work are detailed. The potential implications for future work are briefly covered.

7.1 Research Conclusions

This study aimed to quantify the effects of aligned porous material for face mask applications by demonstrating the process of creating aligned porous nanofiber material and testing it on a non-standard aerosol testing method. The general conclusions can be summarised as follows:

7.1.1 Solution Parameters for Nanoscale Fiber Production

In this work, the appropriate steps were followed to experimentally determine the size of fibers using solution concentration as the leading parameter. Concentrations between 8% to 12% of PCL with CHL and ACT produce nanofibers. The optimal concentration was 10% due to the smooth fibers produced.

7.1.2 Process Parameters for Aligned Fibers

The speed of the collector determined the alignment of fibers. This speed is dependent on the material and printing parameters, primarily voltage. 20% Nylon in FA and 10% PCL in CHL were found to align at collector speeds of 500 and 2000 RPM, respectively.

7.1.3 Environmental Parameters for Porous Fibers

Two methods were utilized to determine parameters to induce porosity in fibers. The solvent mix ratio demonstrated increased pore production only when aided with relative humidity introduced

to the process environment. The introduction of relative humidity alone does not induce pore production. Humidity has an optimal range in which pore production is enabled. This optimal was found for our polymer solvent solution mix at 50% RH.

7.1.4 Aerosol Testing for Face Filtering Masks

The ability to test face filter mask material closely following ASTM 2277 was demonstrated using a simple aerosol testing system. The system produced a distribution of aerosols in the detectable range of 0.3 μm to 5 μm. The system operated stably at 80 L/min at an average velocity of 0.5 cm/s. Pressure drops within the range of 0 to 1000 Pa were captured. Certified N95 masks were tested in this system to verify anticipated filter efficiencies of mask material, confirming an N95 rating. Testing at different system parameters showed confidence in the testing filter materials in particle sizing, flow rate, and air velocity for N95 testing standards.

7.1.5 Filter Efficiency and Pressure Drop of Aligned Porous Nanofibers

PCL fibers' filter efficiency and pressure drop in random, aligned, and porous aligned configurations were tested. Aligned fibers showed the best filtering among the combinations. The porous alignment showed great promise as the pressure drop was significantly less, even with the same material weight as the randomly aligned fiber material. The performance of all combinations achieved less filtration efficiency than existing surgical and N95 mask however had a better lower pressure drop.

7.2 Future Work

The following points lay the groundwork for future work on this topic:

i. Testing an array of multi-feature filter materials could provide insight into which coupled feature could increase the filter efficiency while reducing the pressure drop of filter material.

ii. Investigating the biodegradability while reporting filter efficiency and pressure drop could provide insight into which material would be ideal candidates for mass-production applications.

iii. Investigating the prolonged effect on filter efficiency and pressure drop of repetitively used filter material with multi-feature morphologies could provide insight into the further justification of using multi-feature filter materials.

References

[1] D. Mailley, A. Hébraud, and G. Schlatter, “A Review on the Impact of Humidity during Electrospinning: From the Nanofiber Structure Engineering to the Applications,” *Macromol Mater Eng*, vol. 306, no. 7, p. 2100115, Jul. 2021, doi: 10.1002/MAME.202100115.

[2] J. ’H. Vincent, *Aerosol Sampling: Science, Standards, Instrumentation and Applications*. New York: John Wiley & Sons, 2007.

[3] S. Rengasamy, R. Shaffer, B. Williams, and S. Smit, “A comparison of facemask and respirator filtration test methods,” *J Occup Environ Hyg*, vol. 14, no. 2, pp. 92–103, Feb. 2017, doi: 10.1080/15459624.2016.1225157.

[4] S. C. Kim *et al.*, “Nanofiber Filter Performance Improvement: Nanofiber Layer Uniformity and Branched Nanofiber,” *Aerosol Air Qual Res*, vol. 20, no. 1, pp. 80–88, Jan. 2020, doi: 10.4209/AAQR.2019.07.0343.

[5] K. D. Long, E. V Woodburn Id, I. C. Berg Id, V. Chen, and W. S. Scott, “Measurement of filtration efficiencies of healthcare and consumer materials using modified respirator fit tester setup,” 2020, doi: 10.1371/journal.pone.0240499.

[6] A. Konda, A. Prakash, G. A. Moss, M. Schmoldt, G. D. Grant, and S. Guha, “Aerosol Filtration Efficiency of Common Fabrics Used in Respiratory Cloth Masks,” *ACS Nano*, vol. 14, no. 5, pp. 6339–6347, May 2020, doi: 10.1021/acsnano.0c03252.

[7] N. Scott Deno, E. Kamon, and D. M. Kiser, “Physiological responses to resistance breathing during short and prolonged exercise,” *Am Ind Hyg Assoc J*, vol. 42, no. 8, pp. 616–623, Aug. 1981, doi: 10.1080/15298668191420378.

[8] S. Adanur and A. Jayswal, “Filtration mechanisms and manufacturing methods of face masks: An overview,” *Journal of Industrial Textiles*, vol. 51, no. 3, pp. 3683S-3717S, Jun. 2022, doi: 10.1177/1528083720980169/ASSET/IMAGES/LARGE/10.1177_1528083720980169-FIG2.JPEG.

[9] N. V. Fedorova, “Investigation of the utility of islands-in-the-sea bicomponent fiber technology in the spunbond process,” Oct. 2007, Accessed: Dec. 14, 2022. [Online]. Available: https://repository.lib.ncsu.edu/handle/1840.16/5145

[10] M. D. Calisir, M. Gungor, A. Toptas, U. Donmez, A. Kilic, and S. Karabuga, “Clogging performance of micro/nanofibrous laminated composite air filter media,” *https://doi.org/10.1177/15280837221113084*, vol. 52, p. 152808372211130, Oct. 2022, doi: 10.1177/15280837221113084.

[11] F. Zou *et al.*, “Enhancement of fiber attenuation and filtration quality via electrostatic-induction-assisted melt blowing,” *Textile Research Journal*, vol. 92, no. 21–22, pp. 4147–4162, Nov. 2022, doi: 10.1177/00405175221084279/FORMAT/EPUB.

[12] C. Chen *et al.*, “Study on corona charging characteristic of melt-blown polypropylene electret fabrics,” *J Electrostat*, vol. 121, Jan. 2023, doi: 10.1016/J.ELSTAT.2022.103782.

[13] E. Shim, J. Noh, and Y. Kim, “Development and Performance Evaluation of Polytetrafluoroethylene-Membrane-Based Automotive Cabin Air Filter,” 2022, doi: 10.1021/acsomega.2c04758.

[14] J. Anu Bhushani and C. Anandharamakrishnan, “Electrospinning and electrospraying techniques: Potential food based applications,” *Trends Food Sci Technol*, vol. 38, no. 1, pp. 21–33, 2014, doi: 10.1016/J.TIFS.2014.03.004.

[15] K. Liu, Y. Zheng, M. A. A. Newton, C. Ge, B. Xin, and Y. Xu, “Simulation and experimental study of Taylor cone and jet evolution process parameters in electrohydrodynamics,” *Textile Research Journal*, 2022, doi: 10.1177/00405175221140602/FORMAT/EPUB.

[16] K. R. Dharmarajan, M. Afzaal, Y. S. Tian, E. Q. Li, and S. Thoroddsen, “Mechanism of splitting in Electrospinning,” *Bulletin of the American Physical Society*, 2022.

[17] Y. Salkovskiy and A. Fadeev, “High-efficiency retention of ultrafine aerosols by electrospun nanofibers,” *Scientific Reports* |, vol. 12, p. 20850, 123AD, doi: 10.1038/s41598-022-24739-9.

[18] C. Kuchi, G. S. Harish, and P. S. Reddy, “Effect of polymer concentration, needle diameter and annealing temperature on TiO2-PVP composite nanofibers synthesized by electrospinning technique,” *Ceram Int*, vol. 44, no. 5, pp. 5266–5272, Apr. 2018, doi: 10.1016/J.CERAMINT.2017.12.138.

[19] P. K. Szewczyk and U. Stachewicz, “The impact of relative humidity on electrospun polymer fibers: From structural changes to fiber morphology,” *Adv Colloid Interface Sci*, vol. 286, Dec. 2020, doi: 10.1016/J.CIS.2020.102315.

[20] F. E. Ahmed, B. S. Lalia, and R. Hashaikeh, “A review on electrospinning for membrane fabrication: Challenges and applications,” *Desalination*, vol. 356, pp. 15–30, Jan. 2015, doi: 10.1016/J.DESAL.2014.09.033.

[21] C. J. Luo, M. Nangrejo, and M. Edirisinghe, “A novel method of selecting solvents for polymer electrospinning,” *Polymer (Guildf)*, vol. 51, no. 7, pp. 1654–1662, Mar. 2010, doi: 10.1016/J.POLYMER.2010.01.031.

[22] M. M. Mahmud, A. Perveen, M. A. Matin, and M. T. Arafat, “Effects of binary solvent mixtures on the electrospinning behavior of poly (vinyl alcohol),” *Mater Res Express*, vol. 5, no. 11, p. 115407, Sep. 2018, doi: 10.1088/2053-1591/AADF1F.

[23] L.-G. Liu and J.-H. He, “Solvent Evaporation in a Binary Solvent System for … THERMAL SCIENCE,” vol. 21, no. 4, pp. 1821–1825, 2017, doi: 10.2298/TSCI160928074L.

[24] C. J. Luo, E. Stride, and M. Edirisinghe, “Mapping the influence of solubility and dielectric constant on electrospinning polycaprolactone solutions,” *Macromolecules*, vol. 45, no. 11, pp. 4669–4680, 2012, doi: 10.1021/ma300656u.

[25] L. Liu *et al.*, “Preparation of ultra-low dielectric constant silica/polyimide nanofiber membranes by electrospinning,” *Compos Part A Appl Sci Manuf*, vol. 84, pp. 292–298, May 2016, doi: 10.1016/J.COMPOSITESA.2016.02.002.

[26] J. M. Deitzel, J. Kleinmeyer, D. Harris, and N. C. Beck Tan, “The effect of processing variables on the morphology of electrospun nanofibers and textiles,” *Polymer (Guildf)*, vol. 42, no. 1, pp. 261–272, Jan. 2001, doi: 10.1016/S0032-3861(00)00250-0.

[27] J. Geltmeyer, L. Van Der Schueren, F. Goethals, K. De Buysser, and K. De Clerck, “Optimum sol viscosity for stable electrospinning of silica nanofibres,” *J Solgel Sci Technol*, vol. 67, no. 1, pp. 188–195, Jul. 2013, doi: 10.1007/S10971-013-3066-X/FIGURES/7.

[28] C. J. Angammana and S. H. Jayaram, “Analysis of the effects of solution conductivity on electrospinning process and fiber morphology,” *IEEE Trans Ind Appl*, vol. 47, no. 3, pp. 1109–1117, May 2011, doi: 10.1109/TIA.2011.2127431.

[29] J. Zeng, H. Haoqing, A. Schaper, J. H. Wendorff, and A. Greiner, “Poly-L-lactide nanofibers by electrospinning – Influence of solution viscosity and electrical conductivity on fiber diameter and fiber morphology,” *e-Polymers*, vol. 3, no. 1, Dec. 2003, doi: 10.1515/epoly.2003.3.1.102.

[30] N. Okutan, P. Terzi, and F. Altay, “Affecting parameters on electrospinning process and characterization of electrospun gelatin nanofibers,” *Food Hydrocoll*, vol. 39, pp. 19–26, Aug. 2014, doi: 10.1016/j.foodhyd.2013.12.022.

[31] J. M. Deitzel, J. Kleinmeyer, D. Harris, and N. C. Beck Tan, “The effect of processing variables on the morphology of electrospun nanofibers and textiles,” *Polymer (Guildf)*, vol. 42, no. 1, pp. 261–272, Jan. 2001, doi: 10.1016/S0032-3861(00)00250-0.

[32] N. Bhardwaj and S. C. Kundu, “Electrospinning: A fascinating fiber fabrication technique,” *Biotechnol Adv*, vol. 28, no. 3, pp. 325–347, May 2010, doi: 10.1016/j.biotechadv.2010.01.004.

[33] S. S. S. Bakar, K. C. Fong, A. Eleyas, and M. F. M. Nazeri, “Effect of Voltage and Flow Rate Electrospinning Parameters on Polyacrylonitrile Electrospun Fibers,” *IOP Conf Ser Mater Sci Eng*, vol. 318, p. 012076, Mar. 2018, doi: 10.1088/1757-899X/318/1/012076.

[34] D. P. Ura and U. Stachewicz, “The Significance of Electrical Polarity in Electrospinning: A Nanoscale Approach for the Enhancement of the Polymer Fibers’ Properties,” *Macromol Mater Eng*, vol. 307, no. 5, May 2022, doi: 10.1002/mame.202100843.

[35] A. R. Jabur, L. K. Abbas, and S. M. Muhi Aldain, “Effects of Ambient Temperature and Needle to Collector Distance on PVA Nanofibers Diameter Obtained From Electrospinning Technique,” *Engineering and Technology Journal*, vol. 35, no. 4A, pp. 340–347, Apr. 2017, doi: 10.30684/ETJ.35.4A.5.

[36] A. H. Hekmati, A. Rashidi, R. Ghazisaeidi, and J. Y. Drean, “Effect of needle length, electrospinning distance, and solution concentration on morphological properties of polyamide-6 electrospun nanowebs,” *Textile Research Journal*, vol. 83, no. 14, pp. 1452–1466, Jan. 2013, doi: 10.1177/0040517512471746/ASSET/IMAGES/LARGE/10.1177_0040517512471746-FIG16.JPEG.

[37] N. Kizildag, Y. Beceren, M. Kazanci, and D. Cukul, “EFFECT OF NEEDLE DIAMETER ON DIAMETER OF ELECTROPSUN SILK FIBROIN NANOFIBERS,” 2012.

[38] B. Zaarour, L. Zhu, and X. Jin, “A Review on the Secondary Surface Morphology of Electrospun Nanofibers: Formation Mechanisms, Characterizations, and Applications,” *ChemistrySelect*, vol. 5, no. 4, pp. 1335–1348, Jan. 2020, doi: 10.1002/slct.201903981.

[39] T. Lu *et al.*, “Multistructured Electrospun Nanofibers for Air Filtration: A Review,” *ACS Appl Mater Interfaces*, vol. 13, no. 20, pp. 23293–23313, May 2021, doi: 10.1021/ACSAMI.1C06520/ASSET/IMAGES/LARGE/AM1C06520_0018.JPEG.

[40] C. Huang and N. L. Thomas, “Fabrication of porous fibers via electrospinning: strategies and applications,” *Polymer Reviews*, vol. 60, no. 4, pp. 595–647, Oct. 2020, doi: 10.1080/15583724.2019.1688830.

[41] M. F. Leong, K. S. Chian, P. S. Mhaisalkar, W. F. Ong, and B. D. Ratner, “Effect of electrospun poly(<scp>D</scp> , <scp>L</scp> -lactide) fibrous scaffold with nanoporous surface on attachment of porcine esophageal epithelial cells and protein adsorption,” *J Biomed Mater Res A*, vol. 89A, no. 4, pp. 1040–1048, Jun. 2009, doi: 10.1002/jbm.a.32061.

[42] C. Huang and N. L. Thomas, “Fabricating porous poly(lactic acid) fibres via electrospinning,” *Eur Polym J*, vol. 99, pp. 464–476, Feb. 2018, doi: 10.1016/j.eurpolymj.2017.12.025.

[43] P. Lu and Y. Xia, “Maneuvering the Internal Porosity and Surface Morphology of Electrospun Polystyrene Yarns by Controlling the Solvent and Relative Humidity,” *Langmuir*, vol. 29, no. 23, pp. 7070–7078, Jun. 2013, doi: 10.1021/la400747y.

[44] E. Rezabeigi and N. R. Demarquette, “Ultraporous Membranes Electrospun from Nonsolvent-Induced Phase-Separated Ternary Systems,” *Macromol Rapid Commun*, vol. 40, no. 9, May 2019, doi: 10.1002/marc.201800880.

[45] W. Li *et al.*, “Facile fabrication of porous polymer fibers via cryogenic electrospinning system,” *J Mater Process Technol*, vol. 266, pp. 551–557, Apr. 2019, doi: 10.1016/j.jmatprotec.2018.11.035.

[46] L. Zhu, B. Zaarour, and X. Jin, “Unexpectedly high oil cleanup capacity of electrospun poly (vinylidene fluoride) fiber webs induced by spindle porous bowl like beads,” *Soft Mater*, vol. 17, no. 4, pp. 410–417, Oct. 2019, doi: 10.1080/1539445X.2019.1614060.

[47] E. T. Suryandari, M. A. Zulfikar, R. R. Mukti, and M. Nasir, “Preparation and Characterization of Poly(Methyl Methacrylate) (PMMA) Fibers by Electrospinning,” *Key Eng Mater*, vol. 811, pp. 163–169, Jul. 2019, doi: 10.4028/www.scientific.net/KEM.811.163.

[48] L. Liu, Z. Lin, J. Niu, D. Tian, and J. He, “Electrospun polysulfone/poly(lactic acid) nanoporous fibrous mats for oil removal from water,” *Adsorption Science and Technology*, vol. 37, no. 5–6, pp. 438–450, Jul. 2019, doi: 10.1177/0263617419828059/ASSET/IMAGES/LARGE/10.1177_0263617419828059-FIG8.JPEG.

[49] Y. Tang, Z. Liu, and K. Zhao, “Fabrication of hollow and porous polystyrene fibrous membranes by electrospinning combined with freeze-drying for oil removal from water,” *J Appl Polym Sci*, vol. 136, no. 13, p. 47262, Apr. 2019, doi: 10.1002/APP.47262.

[50] W. Li *et al.*, “Facile fabrication of porous polymer fibers via cryogenic electrospinning system,” *J Mater Process Technol*, vol. 266, pp. 551–557, Apr. 2019, doi: 10.1016/J.JMATPROTEC.2018.11.035.

[51] H. Zhang, L. Zhang, Q. Jia, C. Shi, and J. Yang, “Preparation of porous nylon 6 fiber via electrospinning,” *Polym Eng Sci*, vol. 55, no. 5, pp. 1133–1141, May 2015, doi: 10.1002/PEN.23984.

[52] W. H. Han *et al.*, “Electrospun aligned nanofibers: A review,” *Arabian Journal of Chemistry*, vol. 15, no. 11, p. 104193, Nov. 2022, doi: 10.1016/J.ARABJC.2022.104193.

[53] M. Kashif, H. Guo, J. Ge, X. Lv, S. Rasul, and Y. Liu, “Effect of Different Symmetries of Electrospun Poly(lactic acid) Nanofibers on Facemask Filtration,” *ACS Appl Polym Mater*, vol. 5, no. 8, pp. 5995–6002, Aug. 2023, doi: 10.1021/ACSAPM.3C00696/ASSET/IMAGES/LARGE/AP3C00696_0007.JPEG.

[54] J. P. Feng, J. Wang, W. T. Hwang, and Y. M. Jo, “Characterization of filter media prepared from aligned nanofibers for fine dust screen,” *J Appl Polym Sci*, vol. 136, no. 44, p. 48166, Nov. 2019, doi: 10.1002/APP.48166.

[55] X. Fan *et al.*, “A Nanoprotein-Functionalized Hierarchical Composite Air Filter,” *ACS Sustain Chem Eng*, vol. 6, no. 9, pp. 11606–11613, Sep. 2018, doi: 10.1021/ACSSUSCHEMENG.8B01827/ASSET/IMAGES/MEDIUM/SC-2018-01827C_M003.GIF.

[56] R. Al-Attabi, Y. Morsi, W. Kujawski, L. Kong, J. A. Schütz, and L. F. Dumée, “Wrinkled silica doped electrospun nano-fiber membranes with engineered roughness for advanced

aerosol air filtration," *Sep Purif Technol*, vol. 215, pp. 500–507, May 2019, doi: 10.1016/J.SEPPUR.2019.01.049.

[57] J. Song *et al.*, "Hierarchical Porous Poly(l -lactic acid) Nanofibrous Membrane for Ultrafine Particulate Aerosol Filtration," *ACS Appl Mater Interfaces*, vol. 11, no. 49, pp. 46261–46268, Dec. 2019, doi: 10.1021/ACSAMI.9B18083/ASSET/IMAGES/LARGE/AM9B18083_0008.JPEG.

[58] I. Sriyanti, M. P. Agustini, J. Jauhari, S. Sukemi, and Z. Nawawi, "Electrospun Nylon-6 Nanofibers and Their Characteristics," *Jurnal Ilmiah Pendidikan Fisika Al-Biruni*, vol. 9, no. 1, pp. 9–19, Apr. 2020, doi: 10.24042/jipfalbiruni.v9i1.5747.